Fault locking, block rotation and crustal deformation in the Pacific Northwest

Robert McCaffrey,[1] Anthony I. Qamar,[2,*] Robert W. King,[3] Ray Wells,[4] Giorgi Khazaradze,[2,5] Charles A. Williams,[1] Colleen W. Stevens,[1,6] Jesse J. Vollick[1] and Peter C. Zwick[1,7]

[1]*Department of Earth & Environmental Sciences, Rensselaer Polytechnic Institute, Troy,* NY 12180*, USA. E-mail: mccafr@rpi.edu*
[2]*Department of Earth & Space Sciences, University of Washington, Seattle,* WA 98195*, USA*
[3]*Department of Earth, Atmospheric & Planetary Sciences, Massachusetts Institute of Technology, Cambridge,* MA 02139*, USA*
[4]*U.S. Geological Survey,* 345 *Middlefield Rd.* MS 973*, Menlo Park,* CA 94025*, USA*
[5]*Department of Geodynamics and Geophysics, Universitat de Barcelona, Barcelona, Spain*
[6]*Tele Atlas, 11 Lafayette St., Lebanon* NH 03766*, USA*
[7]*Fugro Seafloor Surveys, Inc.,* 2727 *Alaskan Way, Pier* 69*, Seattle,* WA 98121*, USA*

Accepted 2007 January 29. Received 2007 January 19; in original form 2006 June 6

SUMMARY

We interpret Global Positioning System (GPS) measurements in the northwestern United States and adjacent parts of western Canada to describe relative motions of crustal blocks, locking on faults and permanent deformation associated with convergence between the Juan de Fuca and North American plates. To estimate angular velocities of the oceanic Juan de Fuca and Explorer plates and several continental crustal blocks, we invert the GPS velocities together with seafloor spreading rates, earthquake slip vector azimuths and fault slip azimuths and rates. We also determine the degree to which faults are either creeping aseismically or, alternatively, locked on the block-bounding faults. The Cascadia subduction thrust is locked mainly offshore, except in central Oregon, where locking extends inland. Most of Oregon and southwest Washington rotate clockwise relative to North America at rates of 0.4–1.0 $^\circ$ Myr^{-1}. No shear or extension along the Cascades volcanic arc has occurred at the mm/yr level during the past decade, suggesting that the shear deformation extending northward from the Walker Lane and eastern California shear zone south of Oregon is largely accommodated by block rotation in Oregon. The general agreement of vertical axis rotation rates derived from GPS velocities with those estimated from palaeomagnetic declination anomalies suggests that the rotations have been relatively steady for 10–15 Ma. Additional permanent dextral shear is indicated within the Oregon Coast Range near the coast. Block rotations in the Pacific Northwest do not result in net westward flux of crustal material—the crust is simply spinning and not escaping. On Vancouver Island, where the convergence obliquity is less than in Oregon and Washington, the contractional strain at the coast is more aligned with Juan de Fuca—North America motion. GPS velocities are fit significantly better when Vancouver Island and the southern Coast Mountains move relative to North America in a block-like fashion. The relative motions of the Oregon, western Washington and Vancouver Island crustal blocks indicate that the rate of permanent shortening, the type that causes upper plate earthquakes, across the Puget Sound region is 4.4 $\pm$ 0.3 mm yr^{-1}. This shortening is likely distributed over several faults but GPS data alone cannot determine the partitioning of slip on them. The transition from predominantly shear deformation within the continent south of the Mendocino Triple Junction to predominantly block rotations north of it is similar to changes in tectonic style at other transitions from shear to subduction. This similarity suggests that crustal block rotations are enhanced in the vicinity of subduction zones possibly due to lower resisting stress.

Key words: deformation, fault slip, geodynamics, GPS, tectonics, western US.

[*] Deceased

1 INTRODUCTION

The northwestern United States, adjacent parts of southwestern Canada, and the small oceanic plates offshore are all caught in large-scale dextral shear as the Pacific plate moves northwest at about 50 mm yr^{-1} relative to North America (Atwater 1970; Demets *et al.* 1994). In this region, which we refer to as the Pacific Northwest (PNW), the young, oceanic Juan de Fuca plate subducts northeastward beneath North America at a rate that increases northward from 30 to 45 mm yr^{-1} (Wilson 1993). Along the Oregon coast, subduction is oblique, whereas off Washington and Vancouver Island, subduction is more normal to the margin (Fig. 1). In the far north, off northern Vancouver Island, the oceanic Explorer plate moves independently of both the Pacific and Juan de Fuca plates and converges quite obliquely with northern Vancouver Island (Braunmiller & Nabelek 2002). Juan de Fuca Ridge spreading and the Cascadia subduction zone take up most of the relative plate motion between the Pacific and North American plates, but 20–25% of the motion is broadly distributed within the overriding continental plate. Plate boundary deformation penetrates inland as much as 1500 km, comprising a combination of plate-like regions and deforming zones. Palaeomagnetists have documented progressive, widespread clockwise rotation of the western edge of the region, attributing much of the late Cenozoic rotation to a combination of Basin and Range extension and Pacific-North America dextral shear (e.g. Beck 1976; Simpson & Cox 1977; Magill *et al*. 1982; Gromme *et al*. 1986; Wells *et al*. 1998).

Rotation of the Cascadia forearc is notably different from styles of slip partitioning at some other oblique subduction zones in that the migrating forearc is not clearly defined by strike-slip faulting along or near the volcanic arc, as in the classic example of slip partitioning in Sumatra (Fitch 1972). Global Positioning System (GPS) velocities have been interpreted to show that the forearc, arc and a large part of the backarc is rotating as a single, quasi-rigid body (McCaffrey *et al*. 2000a; Savage *et al*. 2000). Such motion cannot be driven by basal stress derived from oblique subduction

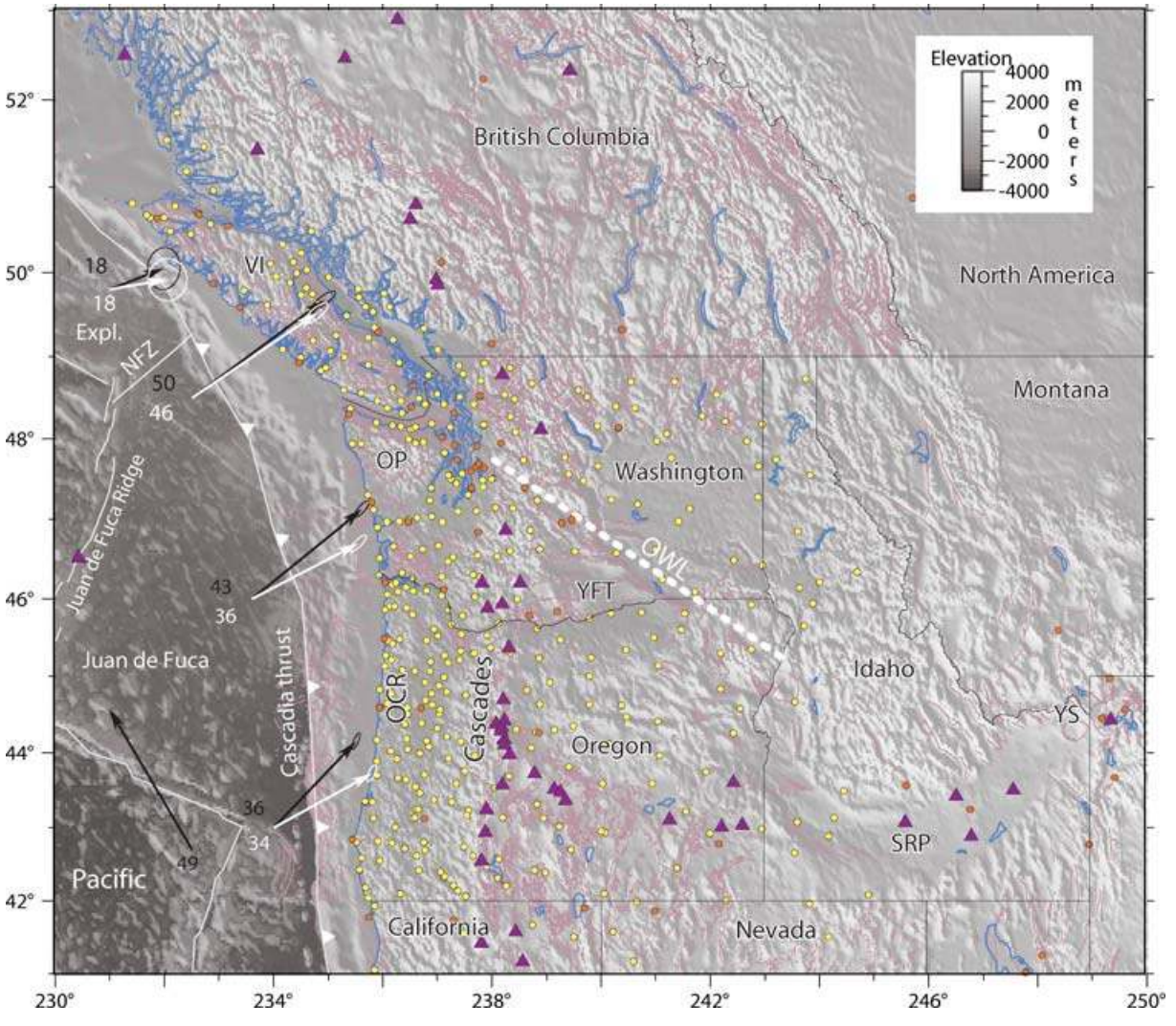

Figure 1. Shaded relief map of the northwestern US and southwestern Canada, with faults (brown lines; from Weldon *et al.* 2003; Massey *et al.* 2005; Washington Division of Geology and Earth Resources staff 2003; US Geological Survey 2006). Arrows at Cascadia deformation front show motion of the Juan de Fuca and Explorer plates relative to North America (black arrows) and relative to the coastal blocks (white arrows). Nearby numbers give the rates in mm yr^{-1}. Triangles represent volcanic centres (Siebert & Simkin 2002) and dots are locations of GPS sites (yellow for survey mode sites, orange for continuous sites; not all sites shown are used in the inversions). NFZ – Nootka Fracture Zone; Expl. – Explorer Plate; OP – Olympic Peninsula; SRP – Snake River Plain; YS –Yellowstone; YFT–Yakima fold-thrust belt; OWL – Olympic Wallowa lineament (white dashed line).

alone, as is inferred for other oblique margins, and must involve other forces. The nature of these forces may be understood better by improving our understanding of the deformation patterns.

Convergence along the Cascadia subduction zone produces repeated large to great earthquakes on the Cascadia megathrust, most recently in the year 1700 (Atwater 1987; Nelson *et al*. 1995; Atwater *et al*. 2005). Documenting the locations and dimensions of the source regions is critical to understanding the possible hazard to the region's inhabitants. Recent palaeoseismological studies reveal additional hazard from shallow crustal faults in the populated Puget Lowland, where large, late Holocene earthquakes have been documented (Bucknam *et al*. 1992; Pezzopane & Weldon 1993; Nelson *et al*. 2003). Clearly, some of the plate convergence and dextral shear is being partitioned into permanent deformation within the upper plate.

To understand better the distribution of deformation, GPS measurements in the PNW began in the late 1980s and have been conducted almost yearly since by several groups. We have processed the available GPS measurements to produce a surface velocity field for the region. We interpret the GPS velocities in terms of strains resulting from the locking of the subducting plates to the overriding plate along the Cascadia thrust, rotations of discrete crustal blocks, and permanent upper plate strain along faults that separate the crustal blocks.

2 GPS OBSERVATIONS AND ANALYSIS

2.1 GPS data

This work combines GPS observations made during the years 1991 through 2004. GPS surveys were conducted in the Pacific Northwest by the Menlo Park office of the U.S. Geological Survey (USGS) from 1991 to 2003 (Murray & Lisowski 2000; Savage *et al*. 2000; Svarc *et al*. 2002). The Cascades Volcano Observatory, also part of the USGS, made measurements in northern Oregon and southern Washington starting in 1992, and the University of Washington (UW) started survey-mode measurements in 1994 (Khazaradze 1999). Yearly from 1996 through 2004, Rensselaer Polytechnic Institute (RPI) surveyed GPS sites throughout Oregon (McCaffrey *et al*. 2000), and since 2001, in Washington in collaboration with UW. In 1998 a collection of county surveyors, universities, and the National Geodetic Survey (NGS) occupied over 150 sites in each of Oregon and Washington, and in 1999, a smaller number in Idaho. We have since re-occupied most of these sites. Processed together with the Oregon, Washington and Idaho GPS observations are those presented by Mazzotti *et al*. (2003) from Vancouver Island and SW British Columbia. In addition to survey-mode data, several continuous GPS sites operate in the region as part of the Pacific Northwest Geodetic Array (PANGA; Khazaradze *et al*. 1999; Miller *et al*. 2001), the Western Canada Deformation Array (WCDA; Dragert & Hyndman 1995), the NGS Continuously Operating Reference Sites (CORS, http://www.ngs.noaa.gov/CORS/cors-data.html), the Basin and Range Geodetic Network (BARGEN; Wernicke *et al*. 2000) and the Bay Area Regional Deformation Array (BARD; http://www.ncedc.org/bard/).

2.2 GPS analysis

To obtain the site velocities (Fig. 2a) from the field data, we follow the procedure described by McClusky *et al*. (2000). First we use the GAMIT software (King & Bock 2004) to combine the phase observations from the field receivers deployed each day with observations from 5 to 10 continuous stations to estimate site positions together with atmospheric, orbital and Earth orientation parameters. We then use the GLOBK software (Herring 2004) to combine these estimates (and their covariance matrices) with estimates obtained from a similar analysis at the Scripps Orbit and Permanent Array Center (SOPAC) (Bock *et al*. 1997) of observations from continuous GPS stations, including all PANGA sites available at the time. In a third step, we aggregate the daily estimates over periods of 10–30 d to reduce the computational burden and to assess better the long-term statistics of the observations. Finally, we combine the ∼monthly averaged position estimates and their full covariance matrices to estimate a long term average site velocity. The velocity solution includes all sites for which the semi-major axis of the 95% confidence ellipse is less than 5 mm yr^{-1}, corresponding to a 1σ east or north uncertainty of about 2 mm yr^{-1}.

The errors in site positions and velocities estimated from GPS observations are a combination of random ('white') and correlated ('red') noise that depends on the satellite and tracking network (both weaker in earlier years); the instrumentation and signal-scattering environment at each site; atmospheric conditions, monument stability and deficiencies in our models for the orbital motions of the satellites, and for site motions due to Earth and ocean tides, and atmospheric and hydrological loading. With the long time-series available for continuous observations, it is possible to reduce the random noise to a negligible level and to evaluate the character of the correlated noise (e.g. Williams *et al*. 2004). For the survey-mode measurements in the PNW, random noise usually dominates. To account for site-dependent noise apparent in the raw (phase) observations, GAMIT estimates an elevation-dependent noise model for each observing session. To account for longer-term errors, we examined the time-series of both the daily and monthly site positions, removing outliers and reweighting the data when high scatter or systematic trends were apparent. In particular, to avoid overweighting the data from permanent stations or field receivers operated every day during a survey, we added quadratically 1.5 mm to the uncertainties of the ∼monthly position estimates for all sites. To account for monument instability and other errors with correlation times of months to years, we included 0.5 mm yr$^{-1/2}$ of random walk noise for all sites, and 2–3 mm yr$^{-1/2}$ for 17 (mostly continuous) sites for which the time-series exhibited significant systematic signatures. Fig. 3 shows histograms of the weighted rms (wrms) and normalized rms (nrms) for all time-series with five or more observations. For both the north and east components, 70% of the wrms scatters are less than 2 mm. The nrms histograms are approximately normal but with a mean at 0.7. Although the error model used for the time-series does not include the random-walk component (we added this only in the velocity solution), a value less than 1.0 is still a reasonable target since we expect the scatter in the time-series to underestimate the true uncertainties in the velocity estimates, which will have a significant contribution from correlated errors.

The GPS velocities are referenced to stable North America using the approach described by Steblov *et al*. (2003), minimizing the horizontal velocities of eight stations (Table 1) with over 10 yr of continuous observations and whose horizontal motion due to glacial isostatic adjustment is likely less than 1 mm yr^{-1}. The wrms of residual horizontal motions of these stations with respect to the North American plate is 0.6 mm yr^{-1}. Alternative approaches (discussed by Steblov *et al*.) and choices of stations used to define the frame result in changes in the velocities of stations in western

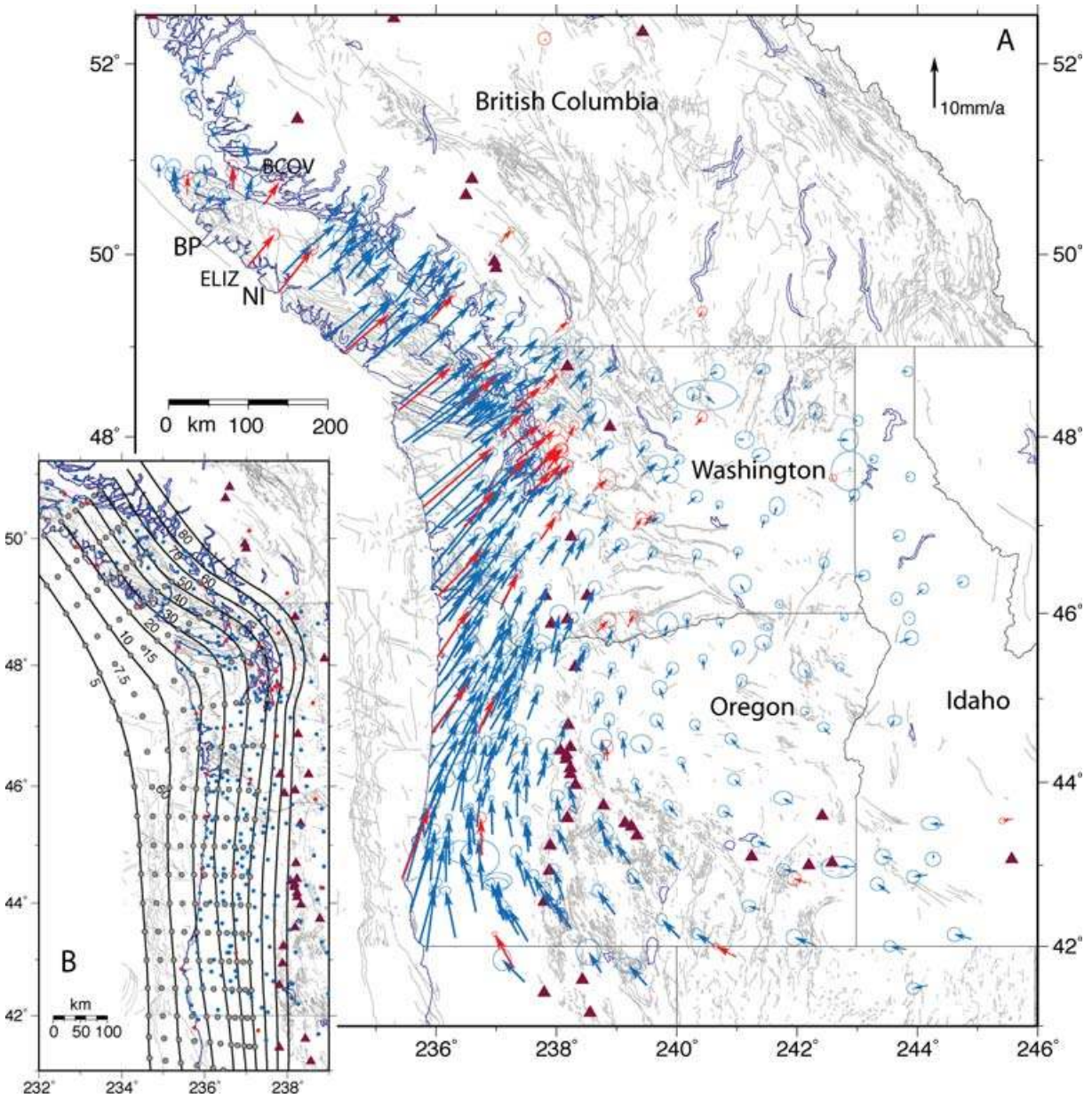

Figure 2. (a) Velocities of GPS sites in North American reference frame. Red vectors are derived from continuous GPS sites, blue from survey mode sites. Error ellipses are at 70% confidence level. Triangles show locations of volcanoes. BP—Brooks Peninsula; NI—Nootka Island; ELIZ and BCOV are continuous GPS sites. (b) Black contours parallel to the coast show depth to the top of the subducting Juan de Fuca plate in kilometres (McCrory *et al.* 2003). Gray dots show locations of fault nodes used in the inversions. Red (continuous) and blue (survey-mode) dots show locations of GPS sites.

Washington of ∼0.5 mm yr^{-1}. During the period of the survey-mode measurements several events produced non-steady motions of the sites: several deep, slow events (Dragert *et al.* 2001; Miller *et al*. 2002) and the February 2001 deep earthquake under Nisqually, Washington. We corrected the affected sites for the 2001 earthquake by using the measured displacements at the continuous sites and the coseismic model of Nabelek & McCaffrey (2001) to estimate the offset at each site. We do not correct for the slow slip events because they are considered to be transient adjustments of the steady creep process.

Obtaining reliable velocities for Vancouver Island presented a particular challenge because almost all of them are based on only two surveys, the first of which was between 1991 and 1994, a time when both GPS receivers and orbital information were much weaker than in later years (Mazzotti *et al.* 2003). In order to assess biases in the early surveys, we compared daily position estimates for survey-mode stations with those from continuous stations operating during the early years, and also velocity estimates for the survey-mode stations with those of nearby continuous stations. Finally, we used the velocity residuals with respect to our models to look for biases that were common to the time of the survey rather than the geometry of the model. We were also aided by comparisons with the Mazzotti *et al.* analysis since they used different software and a different approach to both the analysis and the error model. In the end we were able to obtain almost a factor of two improvement for the velocity accuracies of the survey-mode sta-

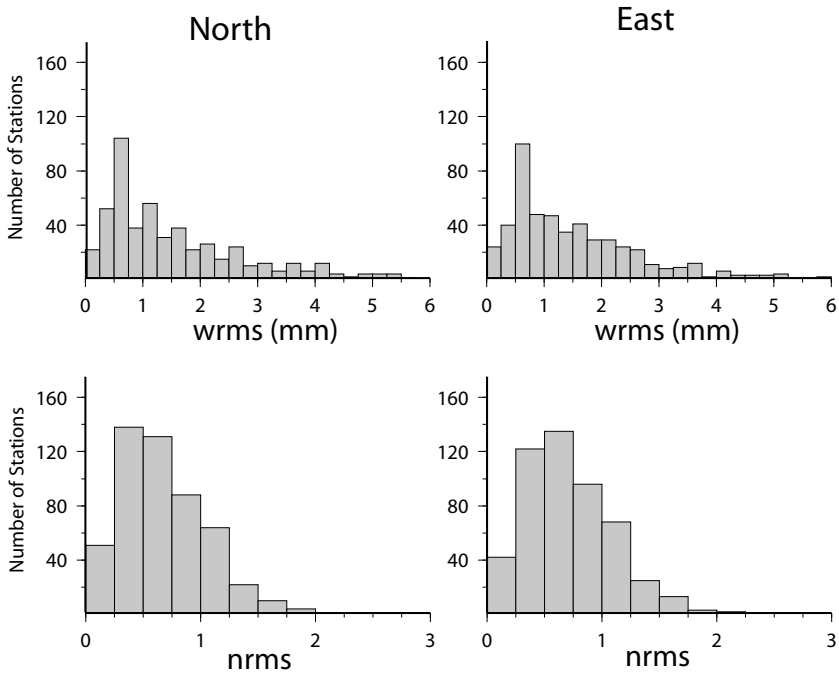

Figure 3. Histograms of the weighted rms (wrms) and normalized rms (nrms) for time-series with five or more observations.

Table 1. Sites used to constrain North America reference frame. Velocities are motions relative to that reference frame.

Site	Longitude	Latitude	*E* velocity (mm yr^{-1})	*E* sigma (mm yr^{-1})	*N* velocity (mm yr^{-1})	*N* sigma (mm yr^{-1})	Rho
STJO	307.32	47.60	0.6	0.8	0.2	0.8	0.00
BRMU	295.30	32.37	0.1	0.5	−0.2	0.5	−0.05
ALGO	281.93	45.96	0.2	0.7	−0.5	0.7	0.00
NLIB	268.42	41.77	0.0	0.3	0.2	0.2	0.03
MDO1	255.99	30.68	−0.4	0.3	−0.5	0.3	0.03
PIE1	251.88	34.30	−0.8	0.8	−0.8	0.8	0.00
YELL	245.52	62.48	0.0	0.2	−0.2	0.2	0.00
WILL	237.83	52.24	−0.4	0.8	0.4	0.8	0.00

tions, with fits to our preferred model of nrms = 0.91 and wrms = 0.7 mm yr^{-1}.

The best test of our noise model is the distribution of the errors in the velocities themselves. To assess these we examine 94 stations in central and eastern Oregon, Washington, and British Columbia, a region that deforms slowly and at long wavelengths. Relative to a simple model that includes locking at the Cascadia thrust and backarc rotation we computed the residual magnitude and its uncertainty for each velocity (Fig. 4a). We then compared a cumulative histogram of the ratio of these values with that expected from a (2-D) chi-square distribution assuming that the north and east residuals are normally distributed with unit variance (Fig. 4b). The histogram shows that our assumed noise model matches the expected distribution of normalized residuals reasonably well: the excess of values to the left of the curve between 50 and 85% indicates that some of the uncertainties are too large; the deficiency above the 95% level reflects the removal of too many outliers. The north component of the residual velocities has an nrms of 1.01, and the east 0.91. For most of the test region, the residuals are randomly distributed, but there are systematic, mostly north–south residuals discernible at the level of 0.5–1.0 mm yr^{-1} for small groups of stations in the NW, NE and SE parts of the region (Fig. 4a). The histogram, component nrms values, and the visible contribution of a N–S model error all suggest that our error model is slightly pessimistic.

3 PACIFIC NORTHWEST GPS-DERIVED VELOCITY FIELD

The GPS velocity field comprises over 500 velocities, including many that are outside the region of the map (Fig. 2) (listed in Supplemental Material). Relative to North America, the GPS-derived horizontal velocities decrease inland, away from the subduction zone, and in Oregon, they show a smooth clockwise rotation of the velocities about a point in the backarc (Fig. 2a). The overall pattern is consistent with the previously recognized large-scale rotation about an axis in eastern Oregon with superimposed plate locking strain (Savage *et al*. 2000; McCaffrey *et al.* 2000a; Svarc *et al*. 2001; McCaffrey 2002). In Washington and SW British Columbia, the vectors are directed to the northeast with the rates diminishing landward—a pattern typical of elastic strain rates resulting from locking on a subduction zone. Northernmost Vancouver Island deviates significantly from this pattern suggesting simple subduction tectonics do not occur there.

We calculate spatial variations in the horizontal principal strain and vertical-axis rotation rates from the GPS velocity field using the spherical deformation gradient tensor approach of Savage *et al*. (2001) and weighted least-squares. We grouped the GPS vectors in overlapping bins of dimensions 2.0° in longitude by 1.6° in latitude and the average strain rates and rotation rates

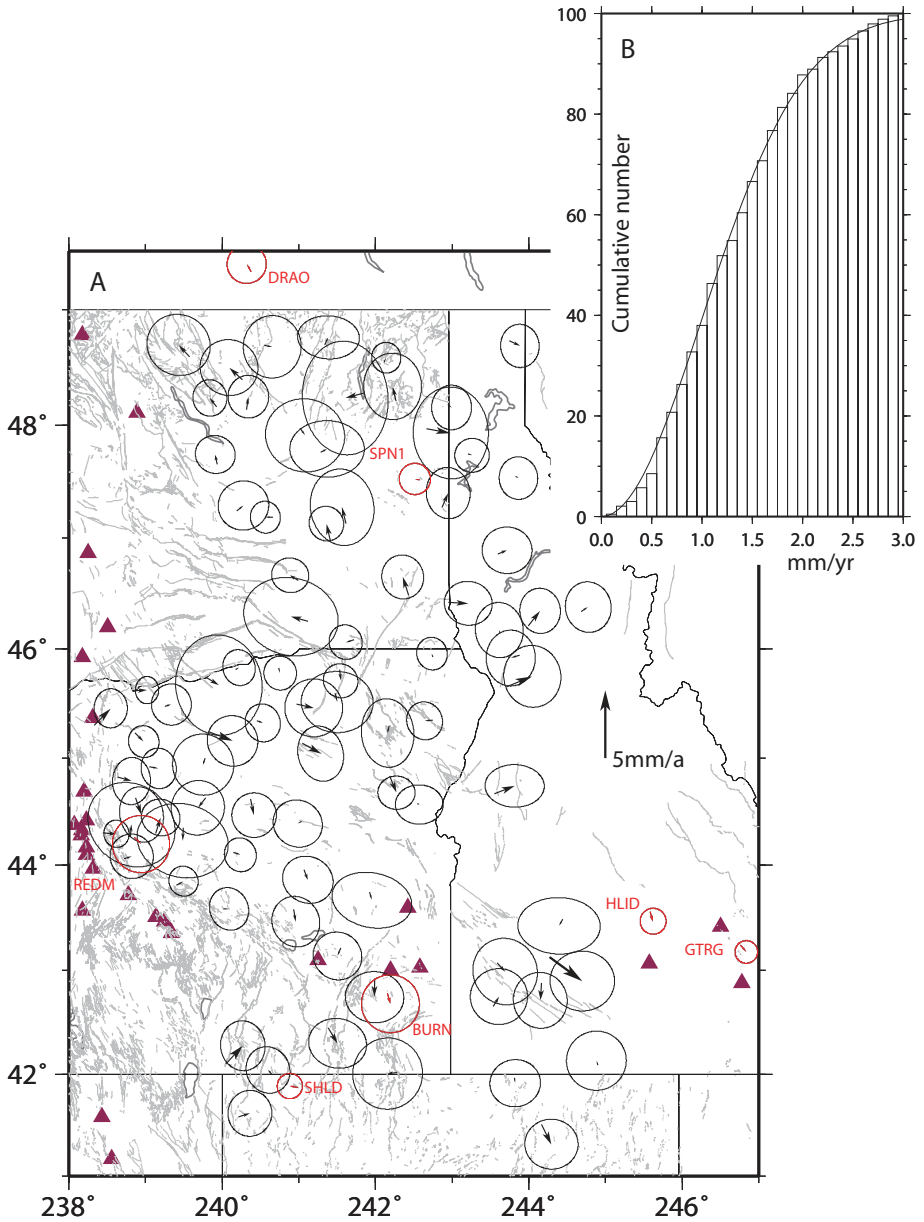

Figure 4. (a) Residual velocities for 94 stations (red for continuous GPS) in the slowly deforming regions of Oregon, Washington and British Columbia, used to validate the GPS uncertainties. All of the stations are located within the domains CIMB, EWas, SnRP, SWId, SEOr and EOre shown in Fig. 6. The model removed includes the subduction thrust and a rotating Oregon block. The velocities for the stations in these six domains are relatively insensitive (<0.2 mm yr^{-1}) to the details of the subduction model. (b) Cumulative histogram of the normalized magnitudes of velocity residuals shown in Fig. 4a. The smooth curve is the theoretical (2-D) chi-square distribution if the north and east residuals are normally distributed with unit variance.

within each bin are estimated along with formal uncertainties (Fig. 5).

Along the coast and extending inland, contraction in the approximate direction of convergence of the Juan de Fuca (JdFa) plate with the coast dominates the strain rate field (Fig. 5a). The surface strain rates decrease eastward away from the coast, suggesting that they are due to subduction of the JdFa plate beneath the coast. In coastal Oregon, the contraction is oriented more perpendicular to the coast than is the convergence of JdFa with North America (NoAm) or JdFa with the coast (Fig. 5a) indicating that some form of slip partitioning occurs. However, the principal axes do not rotate appreciably near the volcanic arc to indicate that shear on an arc-parallel plane occurs there. Instead, the deformation that allows the coastal region to move northward relative to NoAm must occur east of the volcanic arc.

Vertical-axis rotation rates relative to NoAm (Fig. 5b) derived from the GPS velocity field reveal that (1) most of Oregon and SW Washington rotate clockwise at 1 to 2 $^{\circ}$ Ma^{-1} with a decrease in the rotation rate away from the coast; (2) easternmost Oregon, eastern Washington and southern Vancouver Island rotate little and (3) northern Vancouver Island rotates anticlockwise. We address later whether or not such rotations are subduction related. The GPS-derived rapid rotation rates near the coast of Oregon and Washington and their landward decrease are very similar to those revealed in palaeomagnetic declination anomalies (Wells & Heller 1988; England & Wells 1991). This similarity has important implications

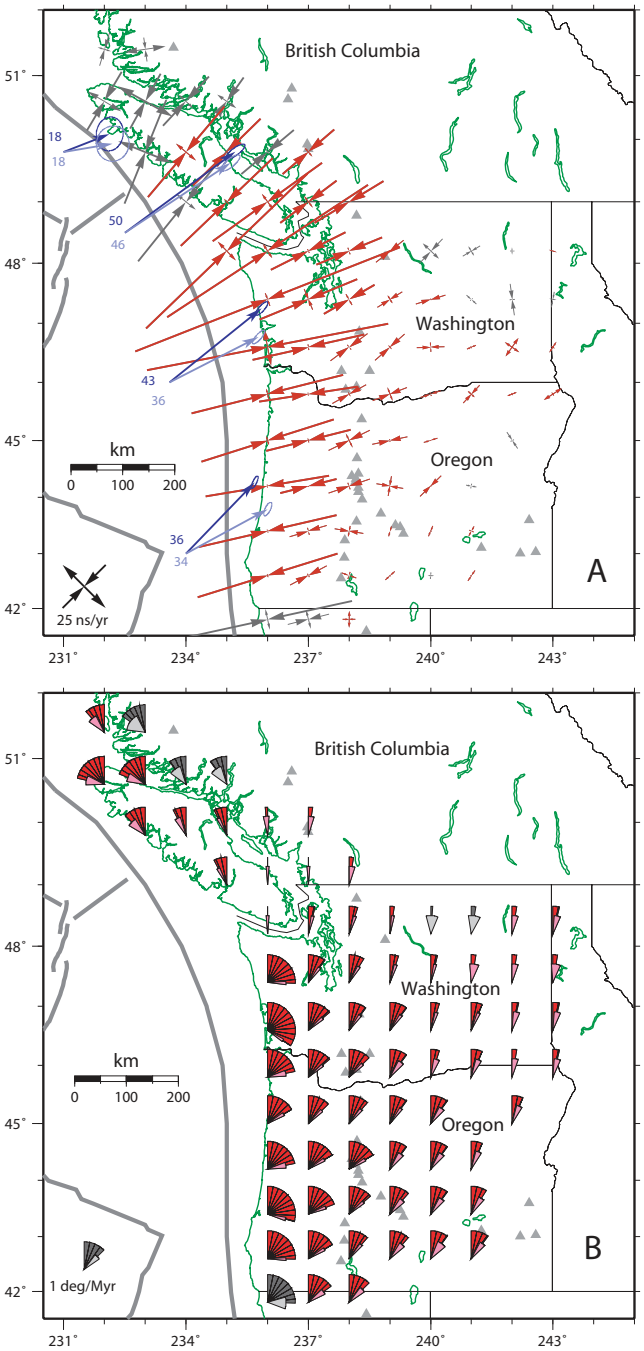

Figure 5. Principal strain and rotation rates derived from GPS velocities. Area is divided into bins of 2° in longitude by 1.6° in latitude in which the uniform strain and rotation rates are calculated from the GPS velocities contained within (minimum of six velocities). (a) Red symbols show principal strain rates where the uncertainty is less than or equal to 5 ns yr^{-1} and grey where uncertainty is between 5 and 10 ns yr^{-1}. Dark blue arrows show convergence of Juan de Fuca with North America, lighter blue arrows are convergence with the coastal blocks; both labelled in mm yr^{-1}. (b) Rotation rates for same regions. Red symbols show where the uncertainty is less than 0.3 ° Myr^{-1} and grey where it is between 0.3 and 0.6 ° Myr^{-1}. Fan symbols show the rate and sense of rotation (a fan opening 45° clockwise indicates 1 ° Myr^{-1} of clockwise rotation). The smaller attached fans show the 1σ uncertainty in the rotation rate.

for whether the strains measured with GPS are elastic or permanent and will be discussed later. The differential rotation of northern Vancouver Island suggests it is a separate crustal block.

The low shear strain rates and high rotation rates indicate that block motions may account for the easterly decrease in the north velocity component across Oregon. Strain rates east of the volcanic arc in Oregon and Washington are small and randomly oriented and do not indicate significant simple shear. If the approximately 10–15 mm yr^{-1} northward movement of the coastal regions relative to eastern Oregon and Washington were due to shear strain on N to NW trending planes, the average strain rate across the 500-km-wide region would be 20–30 nanostrain per year (ns yr^{-1}). The GPS velocity field in Oregon and Washington does not reveal any regions that have close to this rate of shear strain (Fig. 5a). If conversely, such motion were due to plate rotation, the rate would be 20–30 nanoradians yr^{-1}, or roughly 1.0 to 1.5 ° Myr^{-1}. The rotational component derived from the GPS velocity field indeed shows this rate of rotation (Fig. 5b). Because the observed high strain rates are nearly uniaxial contraction in the approximate direction of plate convergence, we conclude that the present day velocity field is largely the result of locking at the Cascadia subduction zone and large-scale rotation of the upper plate relative to North America.

4 INTERPRETATION OF THE VELOCITY FIELD

4.1 Method

We test ideas about the deformation field of the PNW by inverse modelling where we evaluate the roles of block rotations, faults, and distributed permanent deformation. We simultaneously estimate the angular velocities and geographic extent of coherent rotating blocks, the permanent strain within the blocks, and the distribution of locking on the Cascadia thrust and upper plate faults. To do this we use the approach described by McCaffrey (1995, 2002, 2005).

In this work, we define three major plates—North America (NoAm), Juan de Fuca (JdFa) and Pacific (Paci)—along with several smaller plates, that is, the Explorer (Expl) plate and a number of continental blocks. The continental region is initially divided into several discrete geographic *domains* outlined as polygons within the model area (Fig. 6). Domain boundaries are based on knowledge of faulting, seismicity, palaeomagnetic rotations, volcanism and the GPS velocity field. Each tectonic *block* (plate), which may comprise multiple domains if indicated by the data, rotates relative to North America with a specified or estimated angular velocity $\mathbf{\Omega}$. The angular velocity of the Pacific relative to North America is fixed (McCaffrey 2005) and we solve for the angular velocities of the Juan de Fuca and Explorer plates and the continental blocks relative to North America.

Blocks are separated from one another by faults. Elastic strain in the rocks adjacent to the faults can arise if the blocks are in relative motion and the faults are not slipping freely (creeping). This phenomenon is often referred to in the literature as 'locking' or 'coupling'. There is confusion regarding how to describe this feature of faults and what it means physically (e.g. Scholz 1990; Lay & Schwartz 2004; Wang & Dixon 2004). For our purposes we solve for a purely kinematic quantity that represents the instantaneous, spatially averaged creep fraction, denoted by the unitless ϕ. If V is the long-term slip rate on the fault (over many earthquake cycles) and V_c the short-term creep rate (the steady displacement rate across

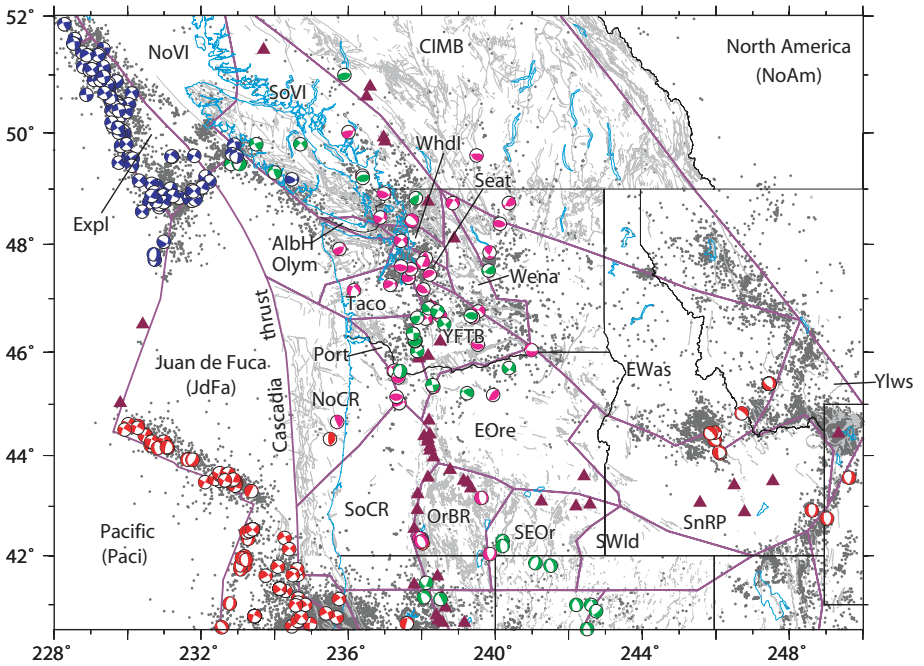

Figure 6. Shallow seismicity (dots; depth <20 km), earthquake focal mechanisms, domain boundaries (purple lines) and faults (thin grey lines) for the Pacific Northwest. Each domain is identified by a four-letter code as described in the text. Red focal mechanisms are from the Harvard CMT catalogue, blue from Braunmiller & Nabelek (2002) purple from miscellaneous sources (see Supplementary Material) green from a compilation by Pezzopane & Weldon (1993) Canadian earthquake quake data from http://www.pgc.nrcan.gc.ca/seismo/recent/eqmaps.html; US quakes from http://www.ncedc.org/anss/catalog-search.html.

the fault surface over a short time), we define

$$\phi(\Sigma) = \Sigma^{-1} \int_{\Sigma} [1 - V_c(s)/V(s)]\, ds, \tag{1}$$

where Σ is a specified patch of the fault surface. By taking Σ to be larger than the characteristic wavelengths of V_c variations we make a continuum approximation to the distribution of ϕ. When $\phi = 0$ the fault is fully creeping and when $\phi = 1$ it is completely stuck. Values of ϕ between those extremes indicate that some parts of the fault creep and some parts do not. In keeping with common usage, we will use the term 'locked' to describe what ϕ represents but note that the fault is probably better thought of as being stuck than locked, since it will become unstuck in the next earthquake or creep event.

In DEFNODE, the computer program that we use, faults that separate the domains are represented in 3-D by nodes distributed on their surfaces. The value of ϕ at each node is then estimated or assigned while the fault slip vector $\boldsymbol{V}$ is calculated from the adjacent blocks' angular velocities. We integrate over the fault surface between the fault nodes by dividing it into small patches (1 km along strike by 0.5 km downdip) and using bilinear interpolation between nodes to get a smooth distribution of $\phi\boldsymbol{V}$ on the fault. We use an elastic half-space dislocation model (EHSD; Okada 1985, 1992) to calculate the surface deformation due to locking on the fault during the interseismic period. Backslip (Savage 1983) is applied to each of the numerous small patches and the surface displacement rates are summed. In the EHSD model, surface velocities are proportional to the quantity $\phi\boldsymbol{V}$, called the slip rate deficit, which has units of velocity. (Sometimes in the literature 'locking' and 'slip rate deficit' are used interchangeably, but here locking, ϕ, is the slip rate deficit per unit slip rate.)

For the Cascadia thrust, ϕ can vary with depth, either by a monotonic decrease (McCaffrey 2002) or by some prescribed function of depth (e.g. Wang *et al*. 2003). We allow the locking to extend as deep as the data indicate. The constraint that ϕ decreases with depth is based on tests that suggest that dislocation models give erroneous surface deformation when there is a downdip increase in ϕV (in general V varies little with depth) (McCaffrey 2002). In addition, Wang *et al*. (2003) make such arguments based on thermal properties of the thrust. Any increase in ϕ with depth is most likely to occur near the deformation front where ϕ is poorly resolved. Variations in along-strike locking values can also be damped, as discussed below.

Permanent (non-elastic) strain rates within the blocks, when applied, are represented by a uniform, 2-D, spherical strain rate tensor (Savage *et al*. 2001). Permanent strain within the blocks is used to account for faulting on scales smaller than can be reasonably represented by discrete domains. Estimation of this strain rate tensor requires an additional three free parameters in the inversion.

4.2 Data

In the inversions, 401 horizontal GPS vectors are used. We use 34 spreading rates (C. DeMets, personal communication, 2005) and 16 earthquake slip vector azimuths (Harvard CMT solutions) from the Juan de Fuca Ridge to constrain Juan de Fuca motion. The Explorer plate's motion is constrained by 75 slip vector azimuths derived by Braunmiller & Nabelek (2002) from regional earthquake waveforms. We use 50 slip vectors for crustal faults obtained from either geological estimates or earthquake fault plane solutions (see Supplemental Material) and 57 vertical axis rotation rates derived from palaeomagnetic declination anomalies (Gromme *et al.* 1986; England & Wells 1991).

We also estimated 24 vertical rates from the GPS data set, but larger uncertainties coupled with a smaller signal renders these much less useful than the horizontal velocities for constraining the model parameters. For the region within 200 km of the coast where we

expect vertical rates to approach 1 mm yr^{-1} or greater, there are five GPS stations (all continuous) with (1σ) uncertainties less than 2 mm yr^{-1}, and 18 others (seven continuous) with uncertainties less than 3 mm yr^{-1}. We include 18 estimates of vertical rates from tide gauge observations (Savage *et al.* 1991; Dragert *et al*. 1994; Mitchell *et al*. 1994) and 11 surface tilt rates estimated from levelling profiles (Hyndman & Wang 1995). We also use 15 horizontal strain rate estimates (Savage *et al*. 1991; Dragert *et al*. 1994; Murray & Lisowski 2000). Because the data set is dominated by the numerous GPS horizontal velocities that have small uncertainties, the vertical data have little influence on the models.

Fault slip rate data derived from geological studies constrain the long-term relative velocities of the blocks across common boundaries. The slip rates are estimated for a particular direction, for example, normal to the fault, and are matched only in that direction. Most inversions presented here include the horizontal GPS rates, slip vector azimuths, fault slip rates and rotation rates. We include the remaining data in a final model (m05A) to show that they generally agree with the inferred final model but do not change it significantly. All data, their uncertainties and predicted values are presented in the Supplemental Material.

Goodness of fit of a particular set of parameters is based on the reduced χ^2 statistic:

$$\chi_{\mathrm{n}}^2 = (N - P)^{-1} \Sigma_{i=1,N}\, p_i, \tag{2}$$

where N is the number of observations, P is the number of free parameters and p is the misfit penalty function whose form depends on the type of data (see appendix 2 of McCaffrey 2005). Models that adequately explain the data, if the uncertainties are properly scaled, will have $\chi_{\mathrm{n}}{}^2 \approx 1$. As another guide, we also compute the probability Q that that the resulting χ^2 for a given model or within a given domain is not due to random chance (Press *et al.* 1989, p. 502). We removed seven GPS vectors with uncertainties larger than 2.5 mm yr^{-1} that add little to the parameter constraints, 18 whose velocities are visibly much different from their neighbours and five near active volcanoes. As we showed above (Fig. 4), the residuals reveal a well-defined probability distribution so those few with large differences are more likely due to causes other than those that one normally uses to assess uncertainties.

4.3 Subduction model

To model the Cascadia subduction zone (CSZ), we use the slab surface defined by McCrory *et al*. (2003) (Fig. 2b). Node positions are the intersections of the slab contours with 20 nearly evenly spaced trench-normal vertical planes.

Beneath northern Vancouver Island (VI) north of the Nootka fracture zone, there is considerable uncertainty whether a downgoing slab exists and if so what its geometry is. Cassidy *et al.* (1998) suggest that the slab extends as a NE-dipping structure to 50°N (beneath the Brooks Peninsula; BP in Fig. 2a). Lewis *et al*. (1997) show that northernmost VI, north and west of the Brooks Peninsula, is quite different from the rest of VI on the basis of heat flow, volcanism and the magnetic and gravity fields. The continuous GPS sites ELIZ on the SW coast at 49.9°N and BCOV on the NE coast at 50.5°N (Fig. 2a) show NE-trending velocities characteristic of the locking evident in the sites to the SE. Sites to the NW of these two have much more northerly trending vectors. Hence we adopt the slab structure of McCrory *et al.* (2003) that truncates the deep slab at the Brooks Peninsula, beneath northcentral Vancouver Island. Northwest of the Brooks Peninsula the Explorer plate was assumed to dip NE at 25° to a depth of 25 km. The southern edge of the Cascadia slab is well south of the limits of our data and its exact location is not important in our modelling. The slab geometry used by Wang *et al*. (2003) differs from the McCrory *et al*. (2003) geometry beneath both Puget Sound and Vancouver Island but only at depths greater than 30 km where there is very little locking evident.

We parametrize the distribution of ϕ on the Cascadia subduction fault in two ways. First, we allow the nodes to be independent of one another except with the constraint that ϕ decreases monotonically with depth along any downdip profile. The second parametrization follows Wang *et al*. (2003) in that $\phi = 1.0$ at depths shallower than the top, z_u, of what they call the effective transition zone (ETZ) and $\phi = 0.0$ at depths below the bottom, z_l, of the ETZ. Within the ETZ

$$\phi(z) = [\exp(-z'/\gamma) - \exp(-1/\gamma)]/[1 - \exp(-1/\gamma)], \tag{3}$$

where $z' = (z - z_u)\,/\,(z_l - z_u)$ and γ is a shape factor. Here, we make a modification to Wang's representation of the depth distribution of locking (eq. 3) to allow for a more general case. Equation (3), in addition to constraining ϕ to decrease with depth, forces the slope $\mathrm{d}\phi/\mathrm{d}z$ to increase or remain approximately constant with depth (see Wang *et al*. their fig. 8). To allow the slope to decrease with depth, we use a new parameter, γ', and make the substitution in (3) of $\gamma = \gamma'$ when $\gamma' \leq 5$, and $\gamma = \gamma' - 10$ when $5 < \gamma' \leq 10$. For values of γ' between 0 and 5, $\phi(z)$ is given by (3) and for γ' between 5 and 10, $\phi(z)$ is (3) reflected about the ϕ and z axes (Fig. 7a).

4.3.1 One-dimensional subduction model

In the initial inversion we allowed ϕ on the Cascadia subduction zone (CSZ) fault to vary only with depth and not along strike. In all estimates of the distribution of ϕ on the subduction thrust, we also allowed the upper plate to comprise several independently moving crustal blocks as discussed below (model m05G). First, values of ϕ at the nodes were constrained to monotonically decrease with depth. When the two shallowest nodes near the deformation front (at 5.0 and 7.5 km depths) were held fixed at $\phi = 1.0$ (curve M1a; Fig. 7a), the inversion resulted in $\chi_{\mathrm{n}}{}^2 = 1.72$ (compared to $\approx$1.10 when along strike variation is allowed, as shown later). The red, dashed curve labelled M1b in Fig. 7a is the result when the two shallowest nodes are allowed to vary but kept at the same ϕ; in this case $\chi_{\mathrm{n}}{}^2 = 1.64$. Another one-dimensional test used the modified *Wang* parametrization in which γ', z_u and z_l were free but not allowed to vary along strike. This model resulted in $\chi_{\mathrm{n}}{}^2 = 1.74$ (blue curve M2a; Fig. 7a) when the fault was fully locked at the surface (Figs 8a and b) and $\chi_{\mathrm{n}}{}^2 = 1.72$ (blue dashed curve M2b; Fig. 7a) when not. The curves are very similar beneath land areas at depths greater than 15 km; the coast generally falls above the 20 $\pm$ 5 km depth contours of the subducting plate, so ϕ at 20 km and deeper appears to be well resolved. ϕ decreases to 10% by 30 km depth. We use the modified Wang parametrization for the remainder of the models discussed here since it gives similar results and has fewer free parameters.

4.3.2 Comparison to CAS3D-2

We tested the fit of the CAS3D-2 Cascadia subduction locking model of Wang *et al.* (2003) by using their slab model and fixing some of the parameters in equation 1 to agree with CAS3D-2. In the CAS3D-2 model, $z_u \approx 10$ km, $\gamma = 0.5$, and z_l was varied along strike. To test the locking model of CAS3D-2 we solved for upper plate block rotations, the locking on crustal faults (model M05h below) and

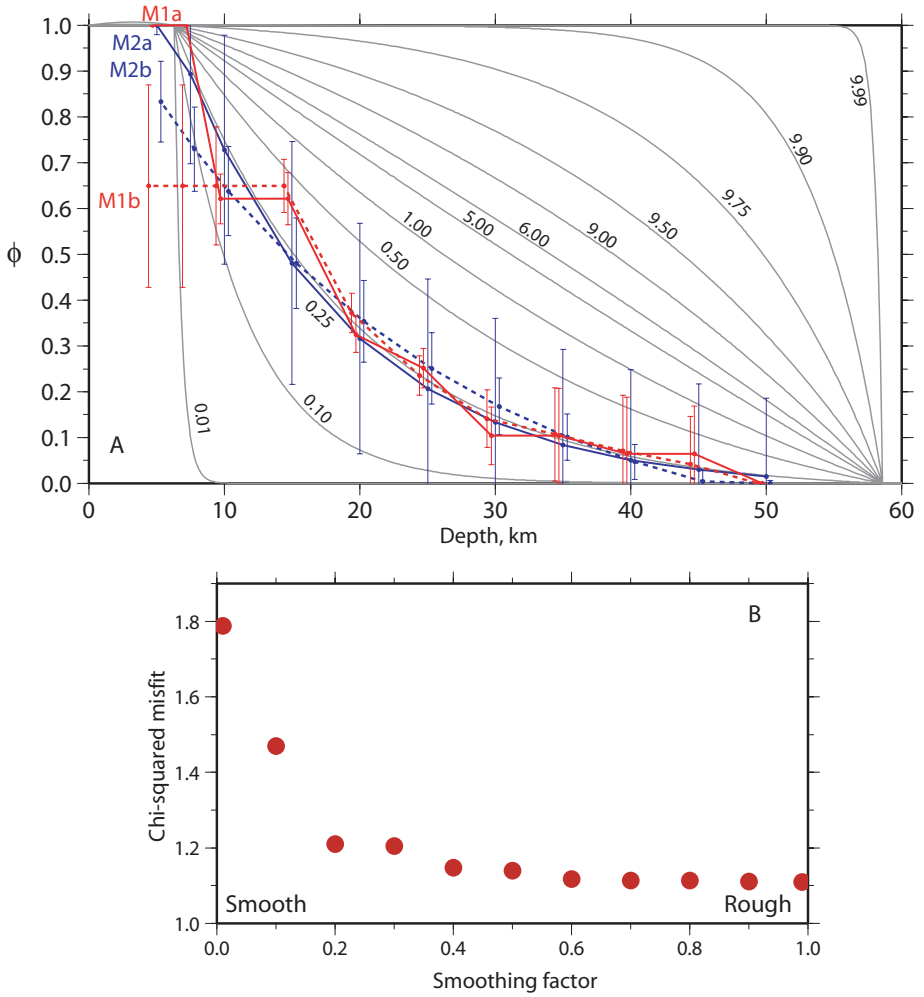

Figure 7. (a) Slip deficit fraction parameter ϕ versus depth for 1-D models. Gray lines are values predicted by eq. (1) as labelled with $\gamma'$and $Z_u = 6.3$ km, $Z_l = 58.6$ km (best-fitting values). Coloured curves are the 1-D slip results in which ϕ varies only with depth. Red curves M1a and M1b curves are for parametrizations where ϕ is constrained to decrease with depth but in no particular form. For M1a, the two shallowest nodes at 5 and 7.5 km are held fixed at $\phi = 1.0$; for M1b these two nodes are free to adjust but are constrained to have the same ϕ. Blue curves show the best-fitting $\phi(z)$ using the modified Wang parametrization. M2a is the result when $\phi = 1.0$ at the surface and M2b (dashed line) is the result when ϕ at the surface is unconstrained. Dots are shown at nodes with 1σ error bars. (b) Reduced chi-squared misfit versus smoothing factor used to smooth along strike variations in ϕ. The factor represents the maximum allowed change in ϕ over 1° (111 km) of distance along strike so larger smoothing factors are 'rougher' models.

z_l while fixing the values of z_u and γ. This inversion resulted in $\chi_n^2 = 1.43$ and a nrms of the GPS velocities of 1.18 ($Q = 0.0$). Hence, the distribution of plate locking in CAS3D-2 does not adequately match the new velocity field.

4.3.3 Along-strike variations in ϕ

The poor fits of the 1-D subduction models indicate that the data contain information about along-strike variations in Cascadia locking. First we examine the inherent smoothness of the along strike variations in ϕ on the Cascadia thrust fault. Along-strike smoothing is applied by limiting the along strike gradient in ϕ (in units of ϕ per degree of distance) to stay below a factor λ by use of a penalty function. Because the nodes are approximately 0.5° apart along strike, $\lambda \geq 2$ represents the undamped solution. For the smoothest (completely damped, $\lambda = 0$) case where ϕ was not allowed to vary along strike (1-D solution), $\chi_n^2 \approx 1.75$ (Fig. 7b). As λ is increased to 0.2 (Figs 7b and 8c,d) the misfit χ_n^2 decreases rapidly and then more slowly to $\lambda = 0.6$ (Figs 7b and 8e,f). For $\lambda > 0.6$ the decrease in χ_n^2 with λ is negligible. A simulation with short wavelength variations in the locking indicates that the data are able to resolve locking variations on the scale of the spacing between nodes (approximately 50 km; Appendix 1 in Supplementary Material). This test and the lack of improved fit at high λ suggest that along-strike locking variations along the Cascadia subduction zone are naturally smooth at this level. In the inversions for the block motions discussed next, we use a smoothing factor $\lambda = 0.6$.

The quantity of interest to earthquake hazards is the slip rate deficit, $\phi \boldsymbol{V}$, where $\boldsymbol{V}$ is the slip vector on the fault (Fig. 8; bottom). $\boldsymbol{V}$ varies along the Cascadia subduction zone due to the rotational nature of the relative plate motions and leads to the differences in appearance of the top (ϕ) and bottom (ϕV) panels in Fig. 8. For example, the high slip rate deficit offshore Vancouver Island in the 1-D model (Fig. 8b) largely disappears in the 3-D model (Fig. 8f). In all cases, the locking estimates for the Cascadia subduction zone indicate that it is largely offshore (Fig. 8). Only in central Oregon and near the Olympic Peninsula does locking of more than about 10% extend below land. Integrating the slip rate deficit over the entire

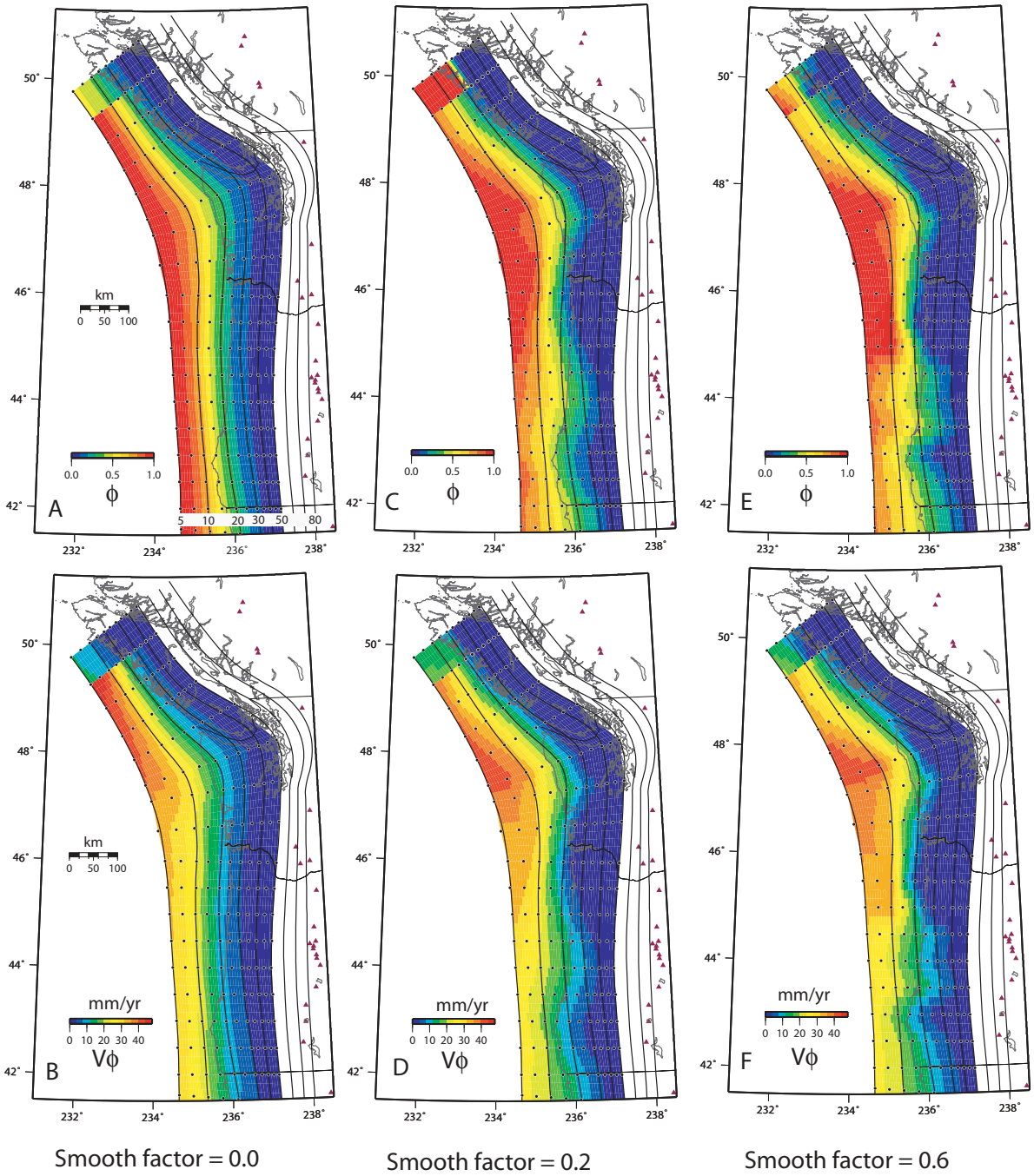

Figure 8. (a, c and e) Distribution of slip deficit fraction parameter ϕ on the Cascadia subduction zone. Dots show the locations of nodes along slab contour lines. In (a) contour lines are labelled in kms. (b, d and f) Distribution of the slip deficit rate on the Cascadia thrust fault for same models as in (a, c and e). Slip deficit rate is the magnitude of the product of ϕ and the predicted relative convergence vector $\boldsymbol{V}$.

Cascadia thrust gives a moment rate of 1.46×10^{20} Nm yr^{-1} which is equivalent to an $M_w = 7.38$ earthquake per year. If this moment buildup is steady over time and released only in large earthquakes, then possible scenarios based on this rate are one $M_w = 8.70$ earthquake every 100 yr, one $M_w = 9.02$ every 300 yr, or one $M_w = 9.22$ every 600 yr.

Satake *et al*. (2003) suggest that the 1700 earthquake had a scalar seismic moment of between 1 and 9×10^{22} Nm (M_w 8.7–9.2). Given the geodetic rate of moment we observe, the recurrence time for the smaller magnitude is 70 and 640 yr for the larger. From turbidites, Goldfinger *et al.* (2003) estimate an average recurrence time of 600 yr but the actual intervals between events ranged from 215 to 1488 yr. While our estimate of the modern day rate of moment build-up, related to elastic strain accumulation, is consistent with the rather broad constraints on the earthquake history of Cascadia, it is not particularly revealing since we do not know that this rate is typical of the earthquake cycle or how the stored elastic strain energy will eventually be released.

The annual rate of moment release in slow quakes from 1997 to 2005 along northern Cascadia is about 1.6×10^{19} Nm yr^{-1} (Tim Melbourne, personal communication, 2006). Since our slip rate deficit model does not correct for these events, our moment rate

estimate does not include the moment released in the slow events. The slow moment release rate is approximately 10% of the total moment rate and may be somewhat higher as there is also evidence for slow-slip events along the southern half of the margin (Szeliga *et al*. 2004).

4.4 Block motions

The GPS velocity field and its spatial derivatives (Fig. 5) indicate that there are a few large regions with low modern strain rates and large rotation rates, suggesting coherent plate-like motions. Here, we test several scenarios of block motions and distributed deformation.

We outlined several crustal domains based on known or suspected faults, seismicity, palaeomagnetic rotations and the GPS velocity field (Fig. 6). The initial domain and fault distributions are more complex than what we expect to resolve with the data; the purpose in starting with a large number of faults and domains is to test hypotheses about which faults are the more important ones in explaining the observations.

Some researchers have alluded to along-strike motion of the Cascadia forearc (Pezzopane & Weldon 1993; Wang 1996; Miller *et al*. 2001) in a manner similar to the classic example of slip partitioning in Sumatra (Fitch 1972). Geologic studies of faulting in Oregon suggest that western Oregon moves northward relative to east Oregon at a few millimetres per year by oblique shear on NNW-oriented faults (Pezzopane & Weldon 1993) and that the arc itself may be extending (Wells *et al*. 1998). However, results of initial GPS work in the PNW suggested that most of Oregon behaves as a rigid rotating block (McCaffrey *et al*. 2000a; Savage *et al*. 2000; Svarc *et al.* 2002). To test for the types of deformation that are indicated by the new data, we present a series of inversions with particular block geometries (only a few are shown here but several more are in the Supplemental Material). Subsequent model refinements are made as warranted by comparisons to the data. We use the probability Q based on the chi-square distribution as a relative guide to the fit of the overall model and to the fits of the GPS vectors within a domain; in general if $Q > 10\%$ we accept the fit as adequate (instead of using $Q > 95\%$ which is more typical) to allow for some non-Gaussian component to the data (see Press *et al.* 1989, pp. 502–503) and because we do not always know how many free parameters are contributing to the fit of the velocities within a single domain. As the model geometry becomes more refined, that is, as we include more independent blocks, more faults in the model become 'active'. For this reason, as additional blocks are added to the model, additional fault and rotation parameters are needed. Additional slip vector and fault slip rate data that define the relative motions of adjacent blocks also become relevant. Some of the test run results are described here and others are described in Appendix 2 of the Supplementary Material in more detail.

4.4.1 Entire region attached to North America

In the run m00r (Fig. 9a) the entire PNW region was held fixed to North America and surface velocities are due only to locking on bounding faults; $\chi_n^2 = 11.1$. In this case the misfits to both the GPS velocities (nrms = 2.8) and slip rates (nrms = 10.7) are large. The slip rate data comprise mostly spreading rates from the Juan de Fuca (JdFa)—Pacific (Paci) plate boundary and are poorly fit because the coastal GPS vectors require a convergence direction that is quite different than that of JdFa—NoAm. The onland GPS data cause the JdFa-Paci pole to change substantially, resulting in a poor fit to the spreading rates. Based on the relatively large Q of the residual GPS velocities within the CIMB domain (≈96%), it is fixed to NoAm. The small domain in southern Vancouver Island, AlbH, also has a large Q suggesting that in this small region the plate locking was capable of matching the few (7) GPS velocities. It is likely that this small domain is part of southern Vancouver Island (SoVI). GPS vectors in the Yellowstone region (Ylws), where ongoing volcanic deformation persists, are not modelled.

4.4.2 Regional-scale rotating blocks

Next we allowed the southern half of Idaho, all of Oregon and western Washington to rotate as a single entity relative to North America (m01r; Fig. 9b) with slip taken up along the Olympic – Wallowa Lineament (OWL – Fig. 1). In addition, Vancouver Island and NW Washington were allowed to rotate separately. Elastic fault strain was included in the faults bounding the rotating blocks. For this model $\chi_n^2 = 1.8$ and the fits to the GPS (nrms = 1.34) and slip rates (nrms = 1.24) were both greatly improved over model m00r. As seen next, the spreading and GPS data can be satisfied simultaneously when the coastal regions are allowed to move relative to NoAm.

4.4.3 Forearc sliver motion

For this run (m03a in Appendix 2) domains west of the Cascade volcanic arc were allowed to move relative to North America by slip along the Cascades arc. The backarc region was fixed to NoAm. This gave a poor fit to the data ($\chi_n^2 = 5.9$) indicating that the forearc domains are not the only regions moving relative to North America.

4.4.4 Multiple rotating blocks

We also examined the fits to the GPS velocities in inversions in which domains were attached to and separated from adjacent domains. From such tests we infer whether or not adjacent domains move together. These tests are based on GPS velocities that have a final wrms of about 0.6 mm yr^{-1} so that when we infer that two blocks move together it is at approximately that level of uncertainty.

4.4.4.1 Oregon and Idaho. Run m01r (Fig. 9b) reveals that the three eastern domains (SnRP, SWId, SEOr) have $Q > 50\%$ when rotating as part of a large coherent region. Subsequent runs (in Supplementary Material) show that these domains and EOre each have $Q > 50\%$ when moving together, suggesting that they move as a single block. The two Oregon forearc domains (SoCR and NoCR) both have $Q > 45\%$ when they rotate together (m03l; Fig. 9c). The OrBR domain has low Q either when attached to SoCR/NoCR or when attached to the composite block to the east. When OrBR is allowed to move independently of the surrounding blocks (m03l; Fig. 9c), the fit to the data is greatly improved; $Q_{\mathrm{OrBR}} \approx 69\%$. Hence the Oregon Basin and Range (OrBR) domain appears to move independently at the mm/yr level from the regions to its east and its west. Hammond & Thatcher (2005) presented GPS velocities and a block model for the region south of 45N. Their inferred block boundaries differ from ours but we note that because the velocities of most of their sites are based on only 3.8 yr of GPS observations, their uncertainties are roughly double ours and our model satisfies their velocities at their quoted level of uncertainty (nrms = 1.08; wrms = 1.3 mm yr^{-1} for model m05A; Fig. 9d).

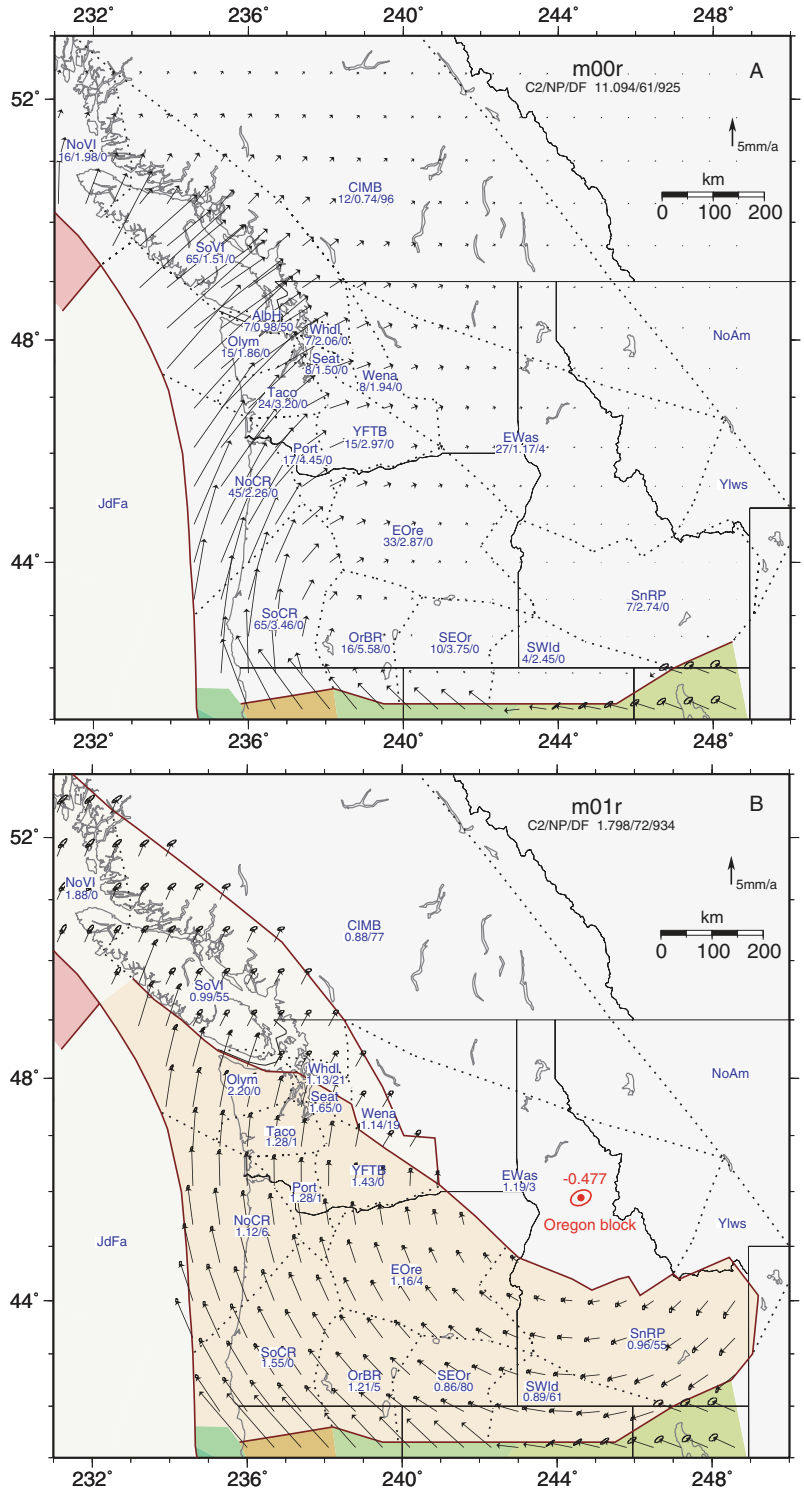

Figure 9. Tests of block boundary models. Model name in upper right, below which is the χ_n^2/number of free parameters/degrees of freedom. In (a) the three numbers below each domain name are the number of GPS vectors, nrms and Q (the probability, in percent, based on the chi-square distribution that the GPS velocities within the domain are satisfied by the model parameters). Contiguous domains that rotate as one are designated by a unique color and are separated by solid red lines that represent faults. Domains that are lumped together are separated by dotted lines. Other than in (a) domains are labelled by four-letter codes, below which are values of nrms for GPS data within the domain and Q. In (a) the entire PNW region is part of North America and the vectors are due to locking on bounding faults (brown lines). In (b)–(d) vectors show predicted rotational velocities relative to North America. Motions of blocks to the south are taken from McCaffrey (2005). Poles of rotation and their 68% confidence ellipses in red are labelled with the rotation rate (in $^\circ$ Myr^{-1}). In (c) and (d), where multiple domains make up a rotating block, the pole is labelled with the name of one of the domains. Poles that are off the map are not shown. OrCR— Oregon Coast Range (domains NoCR + SoCR ± Port). OrId = Oregon – Idaho composite block (domains SWId + SnRP + EOre ± YFTB ± SEOr).

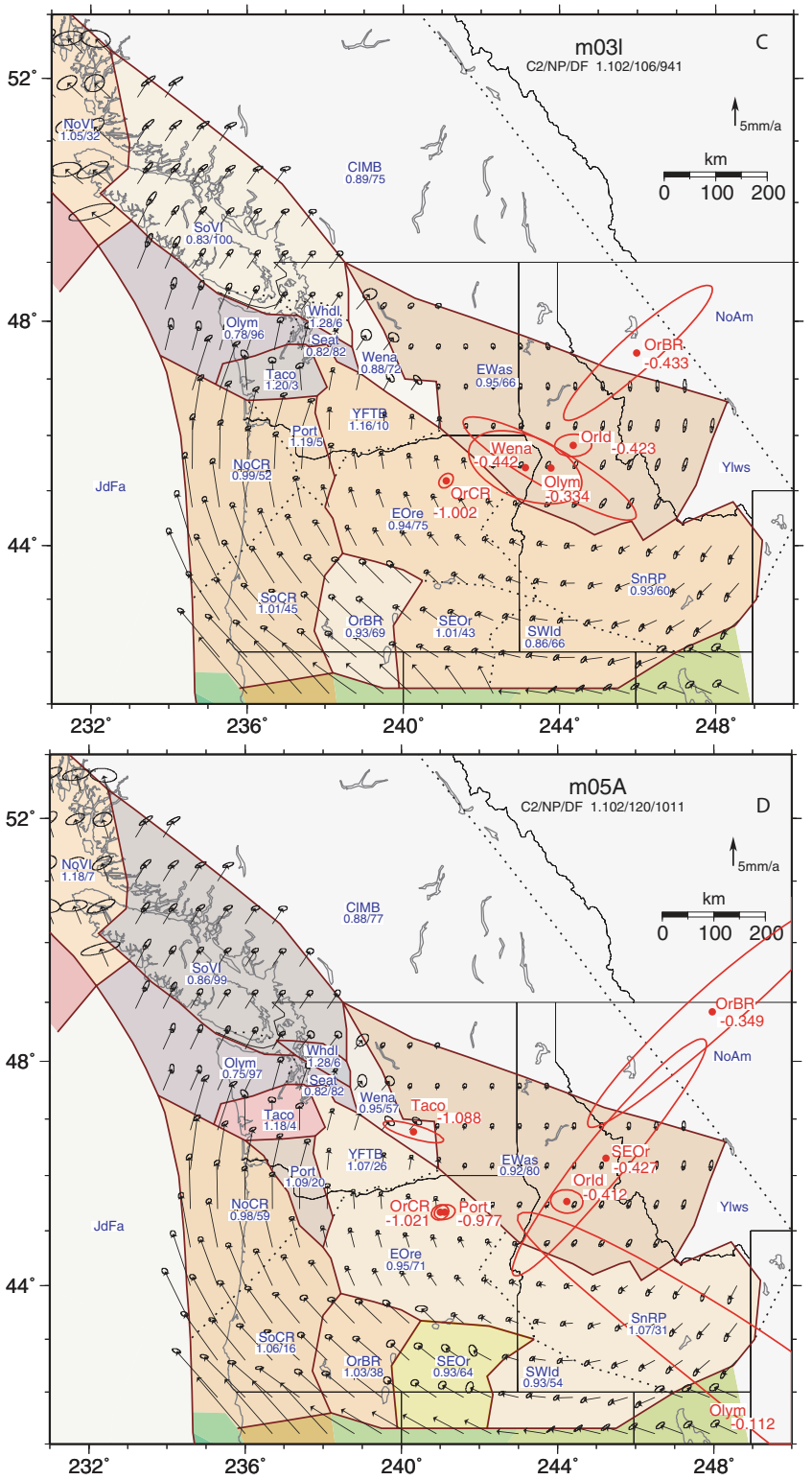

Figure 9. (*Continued.*)

4.4.4.2 Southwestern Washington. In the area of western Washington between the Yakima fold-thrust belt and the Olympic Peninsula, elastic strain rates from the Cascadia subduction zone are large and may mask the strains arising from crustal faults. The rotations of the five domains that make up the Yakima—Puget region are not compatible with a single angular velocity (m03b; Appendix 2). When the Portland domain (Port) is attached to the NoCR/SoCR block, the resulting $Q_{\mathrm{Port}} \approx 5\%$ (m03l; Fig. 9c) suggesting that they may move together. Similarly, an acceptable fit is obtained ($Q_{\mathrm{YFTB}} \approx 10\%$) when the Yakima (YFTB) domain is attached to the large eastern Oregon block (m03l; Fig. 9c). Additional tests suggest that adequate fits are obtained when the Olympic Peninsula (Olym) is

separate from the others or attached only to the Seattle (Seat) domain ($Q_{\mathrm{Olym}} = 75$ to 85%). The Tacoma domain (Taco) has a Q of 5–15% when it is alone, 2–5% when attached to Port and YFTB, and $< 5\%$ when attached to either Olym or the Oregon forearc (NoCR). The Seattle domain (Seat) has $Q = 40$–60% when attached to any of the YFTB, Olym or WhdI domains.

4.4.4.3 Northeastern Washington. The EWas domain, comprising NE Washington and central Idaho, has a $Q < 5\%$ when attached to North America (Figs 9a and b). Letting it move relative to NoAm results in $Q = 66\%$ and a northward motion of 0.7 ± 0.2 mm yr^{-1} (Fig. 9c). This rate is close to the estimated reference frame uncertainty and may be largely reflecting a systematic bias.

4.4.4.4 Vancouver Island and NW Washington north of the OWL. In model m01r (Fig. 9b), where the five domains NoVI, SoVI, AlbH, WhdI and Wena move as a block, one, NoVI, has a significantly lower Q than the others suggesting it moves separately from the southern domains. Allowing NoVI to move separately from NoAm and SoVI improves its Q from < 1 to 28% (m03b; Appendix 2). The improvement in the fit to the SoVI vectors by allowing it to move relative to NoAm is profound, increasing Q_{SoVI} from < 1 to 100% (compare m00r; Fig. 9a to m03l; Fig. 9c).

The Wenatchee (Wena) domain is bounded by the northern edge of the Yakima thrust belt, the OWL in the south, and the Straight Creek fault to the west. When it is attached to North America $Q_{\mathrm{Wena}} < 1\%$; when it moves relative to NoAm as part of the SoVI domain, $Q_{\mathrm{Wena}} \approx 19\%$ (m01r; Fig. 9b); and as a separate block, $Q_{\mathrm{Wena}} \approx 72\%$ (m03l; Fig. 9c). The GPS velocities are not particularly sensitive to the motion of the small domain Whidbey Island (WhdI) since Q is about the same when it is part of Seat to the south or SoVI to the north. Taking into account the tests described (and in Appendix 2), the preferred block model based largely on geodetic data is m03l where most domains have $Q > 10\%$ and overall $\chi_{\mathrm{n}}{}^2 = 1.1$ (Fig. 9c).

4.4.5 Permanent strain within blocks

We test for the role of permanent internal block strain rates by solving for a uniform strain rate tensor within each of eight blocks of model m03l. The run m03m (Appendix 2) with 24 additional free parameters has $\chi_{\mathrm{n}}{}^2 = 0.98$ compared to $\chi_{\mathrm{n}}{}^2 = 1.10$ for m03l that has elastic blocks only. An F-test indicates that this is a better fit at the 98% confidence level. However, the strain rates are small and account for only a small part of the velocity field. Only one strain rate, 9 ns yr^{-1} NE contraction in block Taco, is greater than 5 ns yr^{-1}. For smaller regions, particularly in the Puget Sound area, the geodetic data are not sensitive to whether the deformation is represented by multiple discrete blocks or distributed strain.

4.4.6 Geologic model

In the foregoing, the complexity of the block structure was largely dictated by fits to the GPS velocities since our goal was to see what features of the tectonics are required by the new velocity field. Geologic and seismologic data were included in the inversions but in many cases the overwhelming number of GPS velocities dominated the solutions. Models m05G (Appendix 2) and m05A (Fig. 9d) includes penalty functions to enhance the influence of geologic and seismologic constraints on the solution. In this case, we allow relative motion between any domains that have geologic or seismologic constraints on the bounding fault(s). We also force the parameters to satisfy a number of so-called 'hard data constraints', that is, stiff penalties are applied if the model predicts values for the hard constraints that are outside the specified range. In the final models m05G and m05A all of the hard constraints are satisfied.

The modifications to the block model m03l for model m05G are to (a) separate the SE Oregon (SEOr) block from the others to allow 0.5 to 1.0 mm yr^{-1} fault-normal slip across the Santa Rosa—Quinn—Owyhee fault system (Pezzopane & Weldon 1993), (b) separate the Portland (Port) block from the NoCR/SoCR block across Portland and (c) separate the Whidbey Island block (WhdI) from SoVI to allow a small amount of slip on the Devil's Mountain fault. This inversion results in $\chi_{\mathrm{n}}{}^2 = 1.13$ overall. Poles of rotation for the blocks in model m05G are given in Table 2.

4.4.7 Low weight data

To test the impact of the uplift rates, tilt rates and horizontal strain rates on the final solution, we also ran an inversion of model m05G (called m05A; $\chi_{\mathrm{n}}{}^2 = 1.10$; Fig. 9d) with these 68 additional observations included. The result was largely indistinguishable from m05G while the new data were satisfied within their uncertainties. As shown below, a very slight change in the locking model beneath the Olympic Peninsula coast (where there is little GPS) resulted from the fit to the uplift rates. The following discussion is based on m05A.

4.4.8 Profiles

Some features of the new velocity field are more clearly seen in profiles (Fig. 10). In the profiles of horizontal velocities (Fig. 10a), positive slopes in the red curves, the normal strain component, show extension while negative slopes are contraction. Negative slopes in the blue curves reveal either right-lateral shear or clockwise rotation. One feature that becomes clear is that there is very little, if any, slip across the volcanic arc (shown by grey triangles around X = 300 km) in either the northerly (blue) or easterly (red) velocity components. The strain (red) components of profiles 1 (42°N) and 2 (43°N) both show gentle positive slopes (extension) east of the arc with an overall increase in velocity of about 1 mm yr^{-1} over the 500 km span from $x = 300$ to 800, giving an average extensional strain rate of only 2 ns yr^{-1}. Hence, the GPS results are consistent with very slow extension in the southern Oregon backarc but we cannot determine whether this is a block-type or more distributed style of deformation. Pezzopane & Weldon (1993) describe two or three faults crossed by this profile each of which shows 0.5–1.0 mm yr^{-1} of E-W extension. Hence, the GPS results taken with geologic information suggest that a block-like description of surface deformation is plausible.

Profile 1 (42°N) reveals the possibility of 1–2 mm yr^{-1} of local extension at the arc ($x \approx 280$ km) but this feature is greatly subdued, if present at all, in Profile 2 (43°N) and does not appear in any of the other profiles to the north. Clear offsets at the arc in the north (blue) component are not visible in any of the profiles, ruling out significant strike-slip. However, what is visible at the arc is a change in slope of the north (blue) component which might suggest differential rotation of the forearc and backarc regions. To test whether this change in slope of the north component within the forearc represents plate locking strain instead of rotation, we ran a model where the NoCR, SoCR and Taco domains rotated coherently with the backarc blocks. The resulting large misfit ($\chi_{\mathrm{n}}{}^2 = 1.65$) suggests that plate locking strain is not a satisfactory explanation for this change in slope.

Profile 3 that crosses Oregon at 44°N reveals little if any normal

Table 2. Poles for model M05G relative to North America.

Code	Domain	Long (°E0)	Lat (°N)	ω (° Ma^{-1})	σ_ω (° Ma^{-1})	Max (°)	Min (°)	Az (°)	Block
AlbH	Albert's Head	272.15	14.09	–0.041	0.053	74.9	2.9	147	SoVI
CIMB	Canada Intermontane belt	–	–	–	–	–	–	–	NoAm
EOre	Eastern Oregon	244.54	45.99	−0.406	0.021	0.2	0.2	214	OrId
EWas	Eastern Washington	152.04	26.93	0.008	0.016	113.0	10.4	46	EWas
Expl	Explorer	229.18	52.71	2.937	0.928	1.2	0.6	349	
JdFa	Juan de Fuca	244.66	33.92	–1.513	0.118	1.3	0.2	144	
NoCR	Northern Or. Coast Ranges	240.99	45.16	–1.019	0.036	0.1	0.1	219	OrCR
NoVI	Northern Vancouver Is	261.30	51.75	–0.099	0.294	62.5	5.9	101	
Olym	Olympics	254.50	38.90	–0.126	0.068	12.3	1.2	132	Olym
OrBR	Oregon Basin & Range	248.24	48.75	–0.344	0.075	2.9	0.3	229	
Paci	Pacific	284.16	50.19	–0.761	0.003	0.2	0.2	264	
Port	Portland	241.06	45.19	–0.974	0.038	0.2	0.1	265	
Seat	Seattle	254.50	38.90	–0.126	0.068	12.3	1.2	132	Olym
SEOr	Southeast Oregon	245.61	46.34	–0.424	0.173	3.3	0.3	223	
SnRP	Snake River Plain	244.54	45.99	–0.406	0.021	0.2	0.2	214	OrId
SoCR	Southern Or. Coast Ranges	240.99	45.16	–1.019	0.036	0.1	0.1	219	OrCR
SoVI	Southern Vancouver Is.	272.15	14.09	–0.041	0.053	74.9	2.9	147	SoVI
SWId	Southwest Idaho	244.54	45.99	–0.406	0.021	0.2	0.2	214	OrId
Taco	Tacoma	240.32	46.76	–1.082	0.228	0.7	0.2	105	
Wena	Wenachee	158.76	52.99	0.018	0.202	121.3	12.2	62	
WhdI	Whidbey Island	123.37	34.77	0.030	0.019	103.5	9.3	38	
YFTB	Yakima fold-and-thrust belt	244.54	45.99	–0.406	0.021	0.2	0.2	214	OrId

Long. (Longitude), Lat. (Latitude) and ω (rotation rate) give the rotation pole relative to North America. σ_ω is the uncertainty in ω, Max and Min are semimajor and semiminor axes of error ellipse, Az is azimuth of semimajor axis of error ellipse. Block refers to the composite block to which this domain belongs. The Pacific pole is fixed, taken from McCaffrey (2005).

strain in the arc or backarc regions (flat red curves at $x > 300$ km). West of the arc, ample contraction strain from the subduction zone gives the red curves a large negative slope. Profile 4 crosses the margin at 46°N where contraction in the backarc is starting to be seen and this persists northward in Profiles 5–7. Also northward, the strain rates near the coast increase despite the fact that the coast in the north is farther from the deformation front than it is in the south. For example, compare the margin-normal (red) component at 140 km from the deformation front in Profiles 1 and 7; in Profile 1 it is similar to the baseline value in the backarc while in Profile 7 it is >10 mm yr^{-1} higher than the backarc value. This is why the implied slip deficit rate on the Cascadia thrust in the north is much larger than in the south (Fig. 8; bottom panels).

In Fig. 10 we also compare vertical rates from GPS and tide gauge measurements with the predictions of our models m05G (dashed curves) and m05A (solid curves). Line 7 (vertical) shows a margin-normal profile across the Puget Sound region. Both the GPS and tide gauge estimates match well the ∼3 mm yr^{-1} of differential uplift required to fit the model parameters estimated from horizontal measurements. The bottom panel shows a margin-parallel profile along the coast. Here too the vertical measurements capture the large-scale changes in uplift, but they are not precise enough to discriminate the small-scale variations due to Cascadia locking. The bottom panel also shows that the inclusion of vertical data in m05A influences the model predictions only from 48°N to 49°N (Olympic Peninsula) where horizontal GPS constraints are few.

4.4.9 Fault slip rates

The geologic block model m05G makes predictions of long term slip rates across the block boundaries (faults). Due to the rapid spin rates of several of the blocks, the slip rates are predicted to vary markedly along strike of the faults (Fig. 11) but none of the individual onshore faults slips faster than about 3 mm yr^{-1}. The geologic block model suggests that the convergence of the rotating Oregon coast range OrCR (NoCR and SoCR) block with Vancouver Island is distributed over a region extending from 46°N to 48.5°N. The predicted long-term velocity of the OrCR block relative to North America is 1.8 ± 0.4 mm yr^{-1} east and 6.9 ± 0.2 mm yr^{-1} north measured at Astoria OR, at the mouth of the Columbia River (Fig. 11; inset). About one-third of this is taken up by motion of Vancouver Island and shortening in the Canadian Coast Ranges. About two-thirds, 4.4 ± 0.3 mm yr^{-1}, is likely taken up across Western Washington and the Puget Sound region, between Astoria OR and Bellingham WA (Fig. 11; inset). The case for distributed deformation is supported by the diffuse shallow seismicity between Portland and the Canadian border (Fig. 6). Seismicity rates indicate shortening of 2.9 mm yr^{-1} in this same region (Hyndman *et al*. 2003) although, in our opinion, the catalogue of seismicity is at present both too short and too uncertain to provide a reliable independent estimate of the crustal strain rate.

5 DISCUSSION

5.1 Oregon–North America boundary

The angular velocity of the composite eastern Oregon–southern Idaho block (EOre) relative to North America projects onto the Earth's surface in central Idaho, not far from the inferred boundary of this block with North America (Fig. 9c). The Olympic–Wallowa lineament (OWL; Raisz 1945) is taken as this boundary and the sense of slip predicted by the rotation axis fits with along strike changes in slip for this fault. Southwest of the pole, the NW-trending faults (Long Valley, Pine Valley and Baker; see Pezzopane & Weldon 1993) are normal oblique, characterized by right-lateral slip; faults west of the pole are generally right-slip (La Grande, Wallula, Milton-Freewater, and Arlington-Shuttler faults), and northwest of

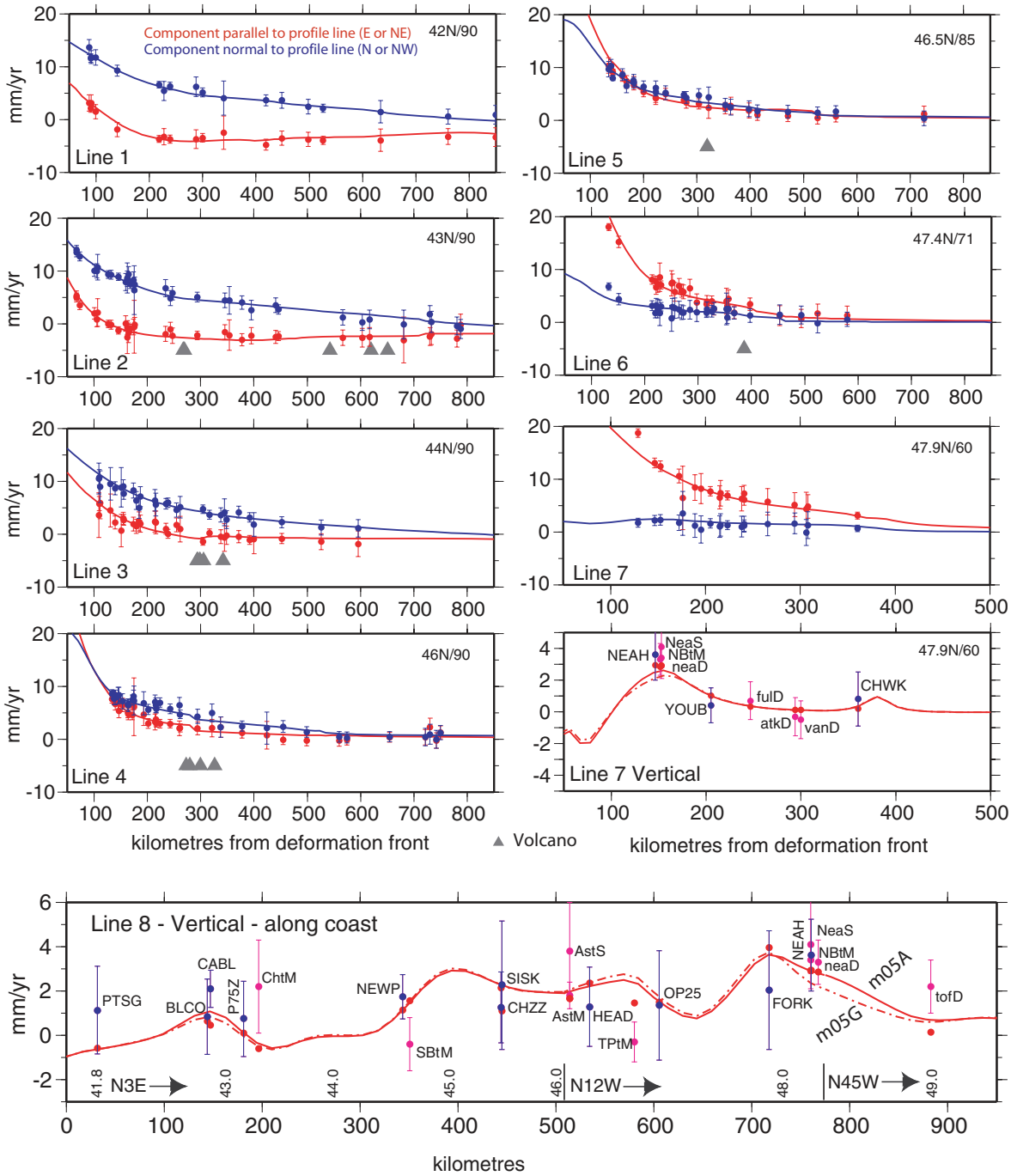

Figure 10. (a) GPS velocities resolved onto profiles shown in Fig. 10b. Red symbols and lines are the observed and calculated GPS, respectively, for the margin-normal component (parallel to the profile line). Blue symbols and curves are for the margin-parallel component of velocity (perpendicular to profile). Error bars are one-standard deviation and grey triangles indicate locations of volcanoes along profiles. Latitude of the west end of each profile at the Cascade deformation front and the azimuth of the profile are shown in upper right. For the panels of vertical rates, observed GPS are in blue and tide gauge in purple. Red curves show predicted values along profiles (solid for model m05A and dashed for m05G); red dots are predicted values at observation points (that may not be directly on profile line). The bottom panel is the coastal profile; approximate latitude is shown on kilometre axis. Vertical tics and directions show changes in the profile orientations. (b) Locations of profile lines as numbered; west end of each profile line is the left side of the panel in Fig. 10a. Line 8 extends northward along coast in three segments as shown.

the pole, faults are contractional (Toppenish Ridge and Saddle Mountain) and right-slip (Kittaitas Valley). The senses of fault slip are consistent with the clockwise sense of rotation of Oregon about a pole northeast of the OWL (Fig. 11).

5.2 Slip along the volcanic arc

We tested for the relative motion of the forearc and backarc regions along the volcanic arc by dividing those regions into separate blocks and solving for their angular velocities. The runs indicate that

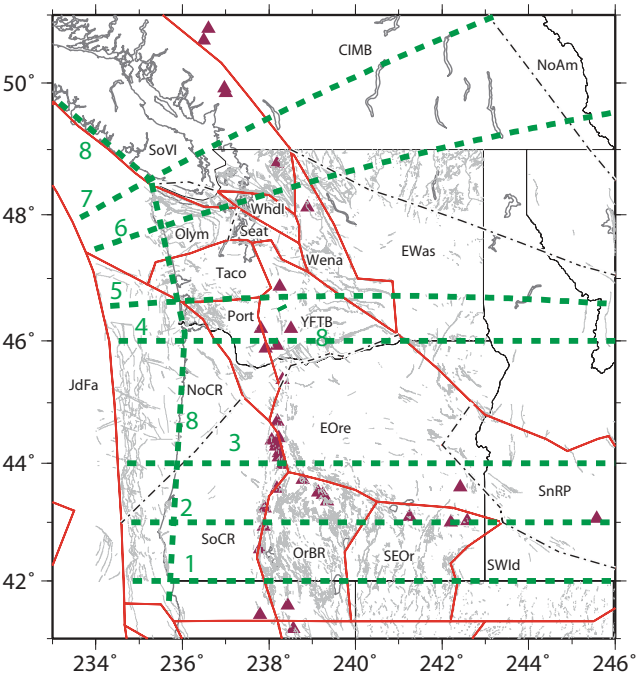

Figure 10 (*Continued.*)

at most the slip rate across the arc is at the mm yr^{-1} level. Profiles of the GPS velocities across Oregon (Fig. 10) reveal no offset in either the arc-parallel or arc-normal component of motion, consistent with the inference of little to no slip along the Cascades. Hence, GPS results indicate that at least over the past decade, internal deformation in the Oregon Cascade arc contributes probably no more than a mm yr^{-1} to the motion of western Oregon relative to North America.

Nevertheless, geologic observations indicate extension across the Oregon Casacde arc over millions of years. The present arc lies within a discontinuous axial graben which initiated at about 4.5 Ma and contains normal faults and abundant basaltic volcanism active in the Quaternary (e.g. Sherrod & Smith 2000). Both volcanism and faulting accommodate the extension in the arc, but the extension rate from geologic data is not well constrained. Conrey *et al*. (2002) estimated late Quaternary extension across the central Oregon arc to be about 1–3 mm yr^{-1}. Wells *et al*. (1998) calculated a Quaternary spreading rate of ∼1 mm yr^{-1} for the central Oregon arc from the heat flow-derived magmatic flux and assuming the present crustal thickness is constant. Our geodetic results are more consistent with the lower rates.

Miller *et al*. (2001) suggest that the lack of apparent slip along the arc in GPS velocities could be caused by elastic strain that arises from plate locking at the Cascadia subduction zone canceling the deformation signal from 'several mm yr^{-1}' of long-term intra-arc extension. We argue against this possibility based on the observation that there is no shear deformation evident along the arc in the GPS results despite the large convergence obliquity. Suppose that the arc is extending rapidly in the E–W direction and that the elastic strain from subduction has the same wavelength and equal and opposite amplitude to cancel it out everywhere along the arc. (This supposition itself is not very strongly grounded as the wavelength of intra-arc deformation is likely on the order of 100 km, much smaller than that of strain from a 300-km-distant subduction thrust; see Prawirodirdjo *et al*. (1997) for an example from Sumatra). Since the locked plate interface does not extend below the volcanic arc, the elastic 'closing' of the arc would require that the eastern edge of the forearc be pushed eastward at exactly the arc opening rate. Because subduction is oblique, the forearc would move northward as well as eastward due to the basal shear of the underlying subducting plate. All along the Oregon coast, the obliquity of subduction of the Juan de Fuca plate beneath the Oregon forearc results in a ratio of approximately 2:1 of the east to north velocities. The localization of strain under a lithospheric stress field requires a local reduction of the effective strength of the crust (Bercovici & Karato 2003; Humphreys & Coblentz 2007). Therefore, the same decrease in strength within the crust of the arc that allows margin-normal strain to localize there will allow margin-parallel shear strain to localize as well. Moreover, this elastic component of margin-parallel shear will not cancel but rather enhance any permanent right-lateral intra-arc shear. Such shear is not observed anywhere along the arc.

We can apply the same argument to counter the notion that intra-arc extension may occur at other times in the seismic cycle; possibly in the decades following a great subduction zone earthquake. Viscoelastic mantle relaxation or post-seismic slip following an earthquake, as has been observed in the Alaska subduction zone (Freymueller *et al*. 2000), produces long wavelength stress changes in the crust, and strain will again localize only if there is a local strength reduction. Episodes of enhanced arc volcanism that sometimes follow great subduction earthquakes possibly due to volumetric pressure changes (e.g. Hill *et al*. 2002) neither require nor imply corresponding episodes of intra-arc extension.

An additional argument against the current locking strain masking the intra-arc extension is that the locking strain rates in S Oregon are much too small to mask any significant extension. For example, in Line 2, along 43°N (Fig. 10), the predicted locking velocity profile (red curve) fits the data west of the arc quite well and shows a rapid strain rate decay toward the arc. From the arc to 100 km to the west, the change in east-velocity (red curve) is 2 mm yr^{-1}. Over the 100 km from the arc east, the change is 0 or 1 mm yr^{-1}. So at the arc, the strain rate from locking is about 1.5 mm yr^{-1} over 100 km. If the arc graben is 70 km wide then the change in E-velocity from locking over this distance is about 1 mm yr^{-1} and this is the most that could be masked.

In summary, the lack of short-wavelength intra-arc shear at the mm yr^{-1} level anywhere along the arc and small elastic strain rates in southern Oregon arc (Fig. 10) suggest that there is neither permanent nor elastic strain localized there at the present time. Present-day intra-arc extension may operate at a mm yr^{-1} or less, at or below the level of the GPS accuracy, and at the lower end of the geologic estimate.

5.3 Rotation of Oregon

The rotations of the crustal blocks are important to constrain since they provide probably our best information about the long-term rate of shortening across the highly populated Puget Sound region where subduction zone strain overprints localized strain from crustal faults. Our current angular velocities for the rotation of the Oregon Coast Ranges (OrCR = SoCR + NoCR ± Port), Eastern Oregon—Southern Idaho (OrId = EOre + SnRP + SWId ± SEOr ± YFTB) and the Oregon Basin and Range (OrBR) regions relative to North America are similar to our earlier estimates (McCaffrey *et al*. 2000a) but differ from that obtained initially by Savage *et al.* (2000). Miller *et al*. (2001) used this difference in pole estimates as evidence against large-scale rotations. Svarc *et al*. (2002) processed and analysed additional data and obtained a refined pole that they interpreted

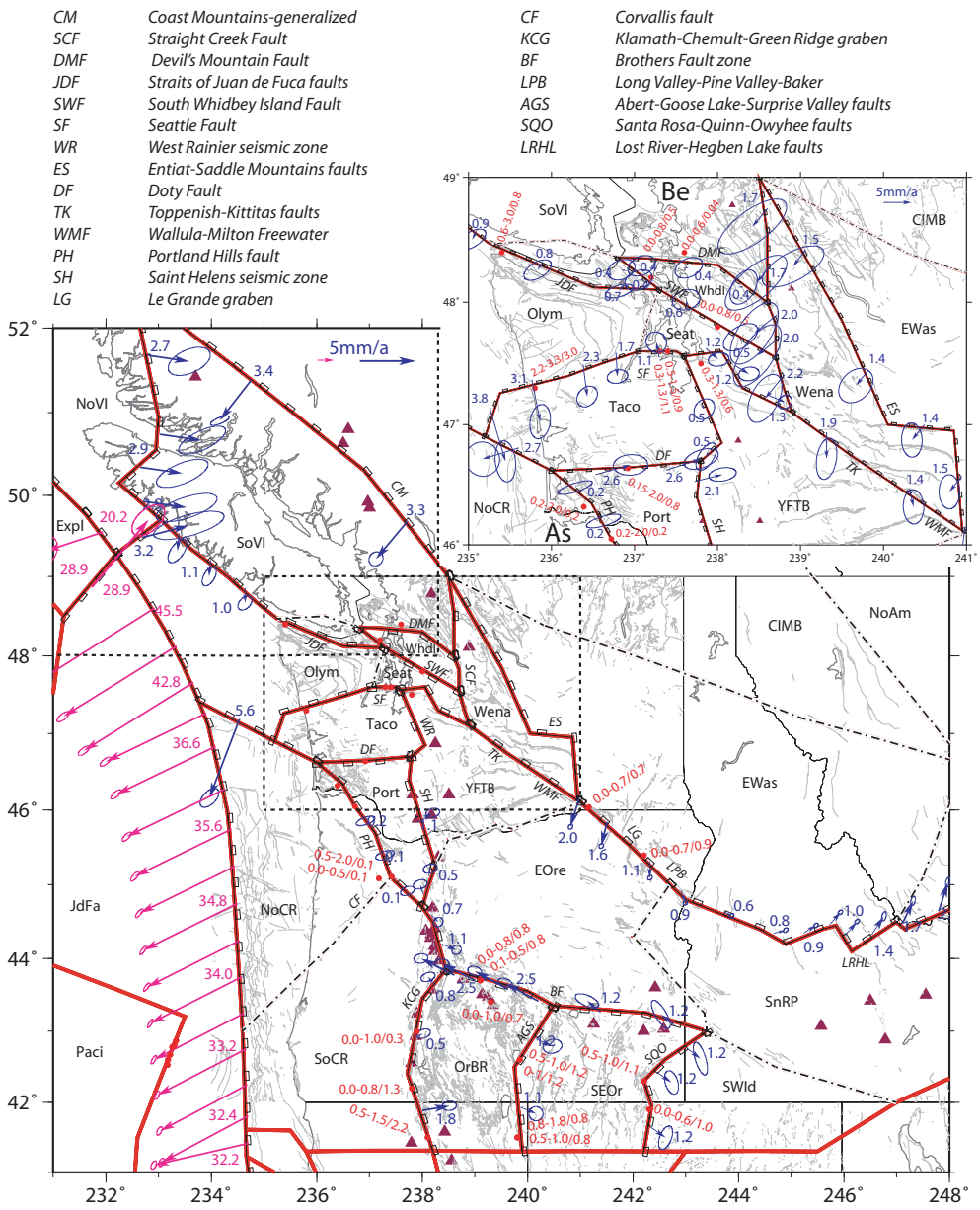

Figure 11. Fault slip rates predicted by model M05G compared to geologic estimates of slip rates. Block-bounding faults are shown as red lines with small rectangles on hanging wall side. Blue vectors show motion of hanging wall relative to footwall with 70% confidence ellipses. Red dots along faults show positions of geologic fault slip estimates. Numbers near them show the range of geologic and model estimates in the form of $V_{\min} - V_{\max}/V_{\text{calc}}$ where $V_{\min}$ and $V_{\max}$ are the minimum and maximum observed values and V_{calc} is the model estimate. Most of the slip rate estimates are fault-normal rates and only this component is matched (as shown). The dashed boxes show the regions of Fig. 11b and 12. (b) Puget Sound region. As—Astoria; Be—Bellingham. Fault name abbreviations given at top.

to be similar to that of Savage *et al*. but again significantly different from ours. Svarc *et al*. (2002; paragraph [15]) suggested that the difference in the poles was due to some bias in our (McCaffrey *et al.'s*) earlier modelling of the impact of elastic strain on estimating the angular velocity. We note instead that the Svarc *et al*. (2002) Oregon–North America angular velocity, though parallel to that of Savage *et al.* is approximately half the magnitude and is actually more similar to ours. Written in their Cartesian coordinates (in units of $^\circ$ Ma^{-1}) $\boldsymbol{\Omega}_{\text{Savage}} = (0.61, 1.05, -1.15)$, $\boldsymbol{\Omega}_{\text{Svarc}} = (0.29, 0.52, -0.56)$, and $\boldsymbol{\Omega}_{\text{McCaffrey}} = (0.35, 0.64, -0.75)$, so that the lengths of the vector differences are $|\boldsymbol{\Omega}_{\text{Svarc}} - \boldsymbol{\Omega}_{\text{Savage}}| = 0.85\ ^\circ$ Ma^{-1} while $|\boldsymbol{\Omega}_{\text{Svarc}} - \boldsymbol{\Omega}_{\text{McCaffrey}}| = 0.23\ ^\circ$ Ma^{-1}.

In this paper, the region incorporated into a single rotating block in those studies (western half of Oregon and southwest Washington) comprises multiple blocks. Our current Oregon Coast Ranges (OrCR) angular velocity (0.35, 0.63, –0.72) points about 1° south of the McCaffrey *et al*. (2000a) Oregon pole but the magnitude of the vector difference is only 0.03° Ma^{-1} and the difference with the Svarc *et al*. pole is 0.20° Ma^{-1}. In terms of the total velocities across the Puget region (Oregon–North America velocity estimated at 237°E, 47.5°N), Savage *et al*. predict 13.9 ± 1.8 mm yr^{-1}, Svarc *et al*. predict 7.6 ± 0.7 mm yr^{-1}, McCaffrey *et al*. (2000) predict 7.0 ± 1.9 mm yr^{-1}, Hammond & Thatcher (2005) predict 6.9 ± 0.7 mm yr^{-1} and this paper predicts 7.1 ± 0.5 mm yr^{-1}. Hence, we

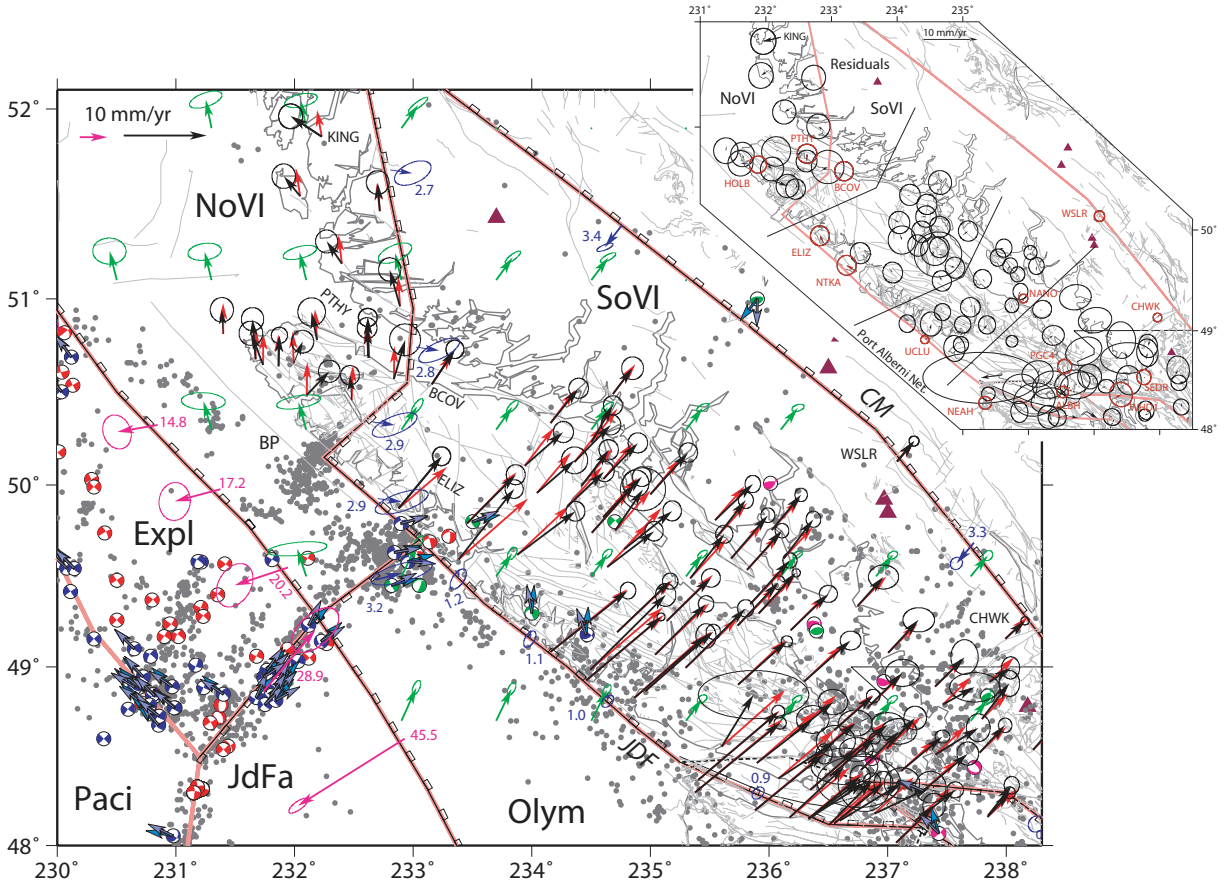

Figure 12. Vancouver Island region. Block-bounding faults are shown as red lines with small rectangles on hanging wall side. Blue vectors show motion of hanging wall relative to footwall with 70% confidence ellipses. Black vectors are observed GPS vectors with 70% confidence ellipses and red are calculated velocities. Purple vectors at the Cascade thrust are at a different scale than those for the on-land faults. Numbers near vectors give slip rates in mm yr^{-1}. Green vectors show motions of the blocks relative to North America. Light blue and dark blue vectors within beachballs show observed and calculated earthquake slip vector azimuths. Gray dots are shallow earthquakes (depth <20 km). (b) GPS velocity residuals. Red vectors are for continuous sites (labelled). Lines separate GPS subnetworks. Fault abbreviations as in Fig. 11.

argue that the outlier in the various estimates of the Oregon – North America angular velocity is the Savage *et al.* (2000) one and not the McCaffrey *et al*. (2000a) one.

5.4 Vancouver Island

When Vancouver Island (VI) is included as part of North America, the result is a systematic northward residual in GPS on the order of 1–2 mm yr^{-1}. This misfit was also noted by Mazzotti *et al.* (2003) who explained it by independent motion of Vancouver Island relative to North America. As shown earlier, we also modelled the entire Vancouver Island as a single block that was allowed to move relative to North America (Fig. 9b), resulting in acceptable fits to the velocities of southern VI sites but still large misfits in the north. Splitting VI into two separate blocks such that the northern end of VI moves independently of the southern two-thirds results in a much better fit to the northern GPS velocities (Fig. 9c). We based our choice of the boundary separating northern and southern VI on the inferred northern edge of the subducting slab, on the notable change in fault density and other geophysical properties west of the Brooks peninsula (Lewis *et al*. 1997) and on the change in GPS vectors from NE-trending to N-trending (Fig. 12). The notable divergence between the two continuous sites BCOV and PTHY in the north suggests that the boundary extends between these two sites. Lewis *et al*. (1997) note that northern Vancouver Island is fundamentally different from the south and that there is evidence for extension in the north. Inversions indicate that the predicted slip along the inferred boundary between north and south VI is nearly E-W extension with northern VI moving nearly due west relative to southern VI (Fig. 12). The lack of fit in inversions described earlier where Vancouver Island was kept a single entity suggests that the change in vectors is not simply a slab edge effect but includes some permanent upper plate deformation. Unfortunately, the geodetic data are too sparse at this time to make any more definitive statements on the tectonics of northernmost Vancouver Island.

The eastern boundary of the SoVI block is uncertain but the relatively rapid (3.2 mm yr^{-1}) NE motions of the continuous sites WSLR and CHWK (Fig. 12) suggests it falls near or east of them. However, there are no nearby GPS sites farther east until DRAO, some 500 km from the subduction zone. How do we know that this is not all elastic loading by the subduction zone? Probably we don't, but tests where Vancouver Island was constrained in its northeastward velocity (v) resulted in larger misfits (where $v = 1.0$ mm yr^{-1}, nrms of SoVI sites $= 1.58$; where $v = 2.0$ mm yr^{-1}, nrms $= 1.14$ and where $v = 3.2$ mm yr^{-1}, nrms $= 0.88$). These tests may be model dependent, since elastic half-space models are quite stiff compared to perhaps more realistic finite-plate models (Williams & McCaffrey

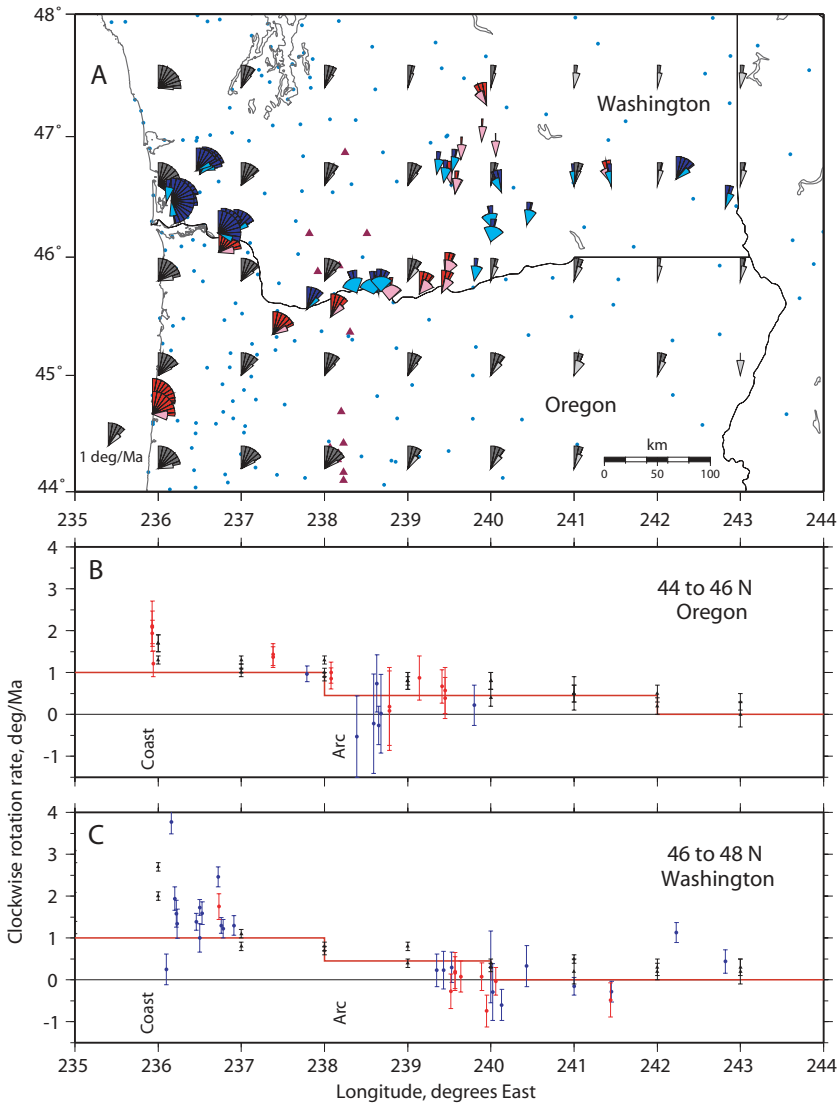

Figure 13. (a) Palaeomagnetic and GPS-derived estimates of vertical axis rotation rates for the Pacific Northwest. The opening of the fan symbol represents the sense and rate of rotation (scale at lower left). Red and blue symbols are from palaeomagnetic declination anomalies from 15 Ma Ginkgo and 12 Ma Pomona flows of the Columbia River Basalt Group (Sheriff 1984; Magill *et al.* 1982) and black symbols are from GPS. The solid-colored wedge is the one-sigma uncertainty. (b and c) Projection of rotation rates onto W–E profiles. Color coding as in (a). Red line shows the rigid body rotation rates for the approximate extents of the blocks. Note that both the palaeomagnetic and GPS-derived rates increase toward the coast.

2001), which predict less rapid landward decay of margin-normal velocities.

On the other hand, Hildreth *et al*. (2003) and Tabor *et al*. (2003) have documented southwestward migration of arc magmatism at the Mount Baker volcanic centre over the past 4 Ma that is consistent with northeast motion of the SoVI block over a deep magmatic source. Assuming a fixed magma source, the inferred block motion is about 6 mm yr^{-1} toward N 40–60°E over the last 4 Ma We estimate 3.3 ± 0.5 mm yr^{-1} towards N42°E from our block model. The southwest younging trend at Mount Baker is part of a coherent pattern in which the Miocene magmatic arc lies northeast of the presently active arc in northern Washington and adjacent British Columbia (Hildreth *et al*. 2003). Although changing slab dip may be entirely responsible, it is simpler to explain the pattern by rotation of the upper plate—an explanation that also applies to the westward displacement of the old arc massif from the presently active arc in Oregon (Wells *et al*.1998).

Palaeomagnetic and modern vertical axis rotation rates

The present-day vertical-axis rotation rate of Oregon relative to North America derived from GPS velocities is about 1.0 ° Myr^{-1} near the coast and 0.4 ° Myr^{-1} in the backarc, both clockwise. These rates are generally consistent with palaeomagnetic declination anomalies in basalts that were erupted 15–12 Ma ago (Magill *et al*. 1982; Sheriff 1984; England & Wells 1991) suggesting the modern rotation of Oregon evident in decadal GPS has been long-lived. The rotation rates in both the palaeomagnetic declinations and GPS velocity field increase by about a factor of 2 within about 50 km of the coast (west of 237°E) (Fig. 13). The similarity of the rotations derived from the different data types and timescales indicates that some component of the deformation in coastal areas recorded by the GPS velocity field is permanent.

Wells & Heller (1988) examined the distribution of rotations in palaeomagnetic data and geologic structures by comparing proposed

mechanisms for rotation. They ruled out significant rotations during the oblique docking of the Oregon Coast Ranges (Simpson & Cox 1977). Based on an estimate of the post-15 Ma extension in the northern Basin and Range, they concluded that the rotations in the Oregon forearc were driven in part by Basin and Range extension and in part by margin-parallel shear in the Oregon forearc.

The agreement of the modern rotation rates with the palaeomagnetic estimates supports the Wells & Heller (1988) interpretation. The palaeomagnetic rotation rate near the coast is about 1 $^\circ$ Myr^{-1} faster clockwise than the rotation of the rigid Oregon forearc as a whole (Fig. 13). If this excess rotation is due to blocks caught in a shear zone, the rotation rate is either the same as or one-half the shear strain rate, depending on the mechanism driving the rotation (McKenzie & Jackson 1983). A vertical axis rotation rate of 1° Myr^{-1} is equivalent to 17 nanoradians yr^{-1} so the shear strain rate causing the rotation is either 17 or 34 ns yr^{-1}. For a 50-km-wide deforming zone, this shear strain rate results in a velocity difference of 0.8–1.7 mm yr^{-1} across it. Hence, there could be as much as 1.7 mm yr^{-1} of permanent coast-parallel shearing along the Cascadia margin.

If the coastward increase in the rotation rate is due to a coastward increase in the simple shear strain rate then a similar magnitude velocity gradient should be evident in the strain rate tensor as well. The GPS velocity field reveals a shear strain rate $\varepsilon_{\mathrm{EN}} = -18 \pm 2$ ns yr^{-1} along the coast (236E) from 42 to 47N (right-lateral shear parallel to the coast). In the same region the excess rotation is $1.2 \pm 0.5^\circ$ Myr^{-1}, about 20 nanoradians yr^{-1}, consistent with simple right-lateral shear on N–S planes.

Late Cenozoic faults mapped in the Coast Range of southwest Washington (Wells 1981, 1989) and northwest Oregon (Wells *et al.* 1995) form 'bookshelf-style' domains of WNW left-lateral faults bounded by through-going, NNW right-lateral faults consistent with dextral shear deformation. The spacing of the faults and the strike-slip rate on them can be used to estimate the rotation rate (Freund 1974). Wells & Coe (1985) used this method to calculate that the fault geometry and apparent offsets could accommodate observed late Cenozoic clockwise rotations in southwest Washington, but uncertainties in fault slip did not permit resolution of the rigid plate component. Similar WNW-trending left-lateral strike-slip faults may accommodate rapid bookshelf-style clockwise rotation in offshore Oregon (Goldfinger *et al.* 1992, 1996), where the faults are spaced about 40 km apart and are slipping at 5–6 mm yr^{-1}. Dividing 6 mm yr^{-1} by 40 km gives a rotation rate of 15 nanoradians yr^{-1}, which is nearly 1 $^\circ$ Myr^{-1} and roughly equivalent to the excess rotation rate seen in the GPS and palaeomagnetic data.

5.6 Transition from California shear to Oregon rotations

In northern California, crustal blocks move relative to North America largely by shear along rapidly-slipping NW-trending faults (Fig. 14). In the Walker Lane belt that separates the Sierra Nevada block from the Basin and Range (Fig. 14), similar shear strain occurs but likely in a more distributed fashion (Hammond & Thatcher 2005). From block models of western US deformation McCaffrey (2005) found that the angular velocities for blocks in northern California (south of Mendocino triple junction; MTJ) pointed far from the blocks and therefore produced relatively small velocity gradients across them. In this case the change in velocity across the deforming zone is largely accommodated by faulting. North of the MTJ, the blocks rotate about nearby axes resulting in large rotational velocity gradients and the role of faulting is relatively minor. At this point the details of this transition, in terms of the deformation required, are not clear. However, the overall pattern appears to be similar to at least one other transition from transform faulting to subduction, that is, in New Zealand. There, rapid rotations occur in the North Island forearc of the Hikurangi subduction zone (Wallace *et al*. 2004) while blocks in the adjacent Marlborough region of the northern South Island, where strike-slip faulting predominates, rotate slowly about distant axes (Wallace *et al*. 2006).

5.7 Vertical axis rotations, faulting and escape

In zones of distributed deformation, very often vertical axis rotations of crustal blocks can account for velocity gradients that would otherwise require faulting. A nice example of this, as noted above, is in the North Island of New Zealand, where the geometry of oblique plate convergence and slip partitioning predicted much larger components of strike-slip faulting than geologists were able to recognize in active faults (e.g. H. Wellman 1983, unpublished manuscript, cited by Nathan 2005). However, it has recently been noted that rotations can take up approximately two-thirds of the required velocity gradients, and therefore the combination of known faulting rates and rotations can satisfy the total change in margin-parallel velocity across the North Island (Wallace *et al*. 2004). By contrast, in southern California, it appears that rotations play a very small role relative to faulting (McCaffrey 2005).

In Oregon, rotations account for most, possibly >90%, of the northward motion of the coast relative to North America and very little faulting is required. The northward transition from shear faulting in northern California and Nevada to rotation in Oregon occurs over a short distance (Fig. 14) and coincides with the transition from a strike-slip to a subduction plate boundary. Wallace *et al.* (2005) have shown in a global study of regions of rapid block rotations constrained by geodetic and palaeomagnetic data, that rapid rotations are commonly associated with subduction zones. One might expect the low resisting stress of the subduction zone to allow so-called 'tectonic escape' to occur (Humphreys & Hemphill-Haley 1996; Mann 1997). However, in the case of Cascadia, the pole of rotation of the forearc (OrCR; Fig. 9d) is south of the latitudinal midpoint of the subduction zone—this results in a net flux of the forearc crust eastward rather than westward relative to North America. Hence, the ultimate fate of Oregon is not to escape from the zone of deformation but instead to rotate and collide with North America across the Puget Sound region. Perhaps low resistance of the subduction zone allows the rotations to occur or that differential along-strike subduction stress may drive the rotations.

Wallace *et al.* (2005) propose that collision of a buoyant feature on the subducting plate with the forearc can lead to rapid rotations of forearc blocks by causing differential subduction rates along strike. While no such collision occurs at Cascadia, a similar effect may result from the proposed rapid, 3 mm yr^{-1}, E–W shortening within the Olympic Mountains (Pazzaglia & Brandon 2001). A test of this mechanism, proposed by Wallace *et al*. (2004, 2005), is that the poles of rotation of the rotating upper plate blocks relative to the subducting plate intersect the surface of the Earth near the point of collision. The pole of rotation of the Oregon Coast Range (OrCR) block relative to the Juan de Fuca plate (near 249.9E, 12.3N, $\omega = 0.55^\circ$ Myr^{-1}) is very far from the Olympic Peninsula and therefore does not pass this test.

In the most general terms the deformation of the Pacific Northwest is driven by interaction of the Pacific plate with North America (Atwater 1970) and gravity acting on spatial variations of density

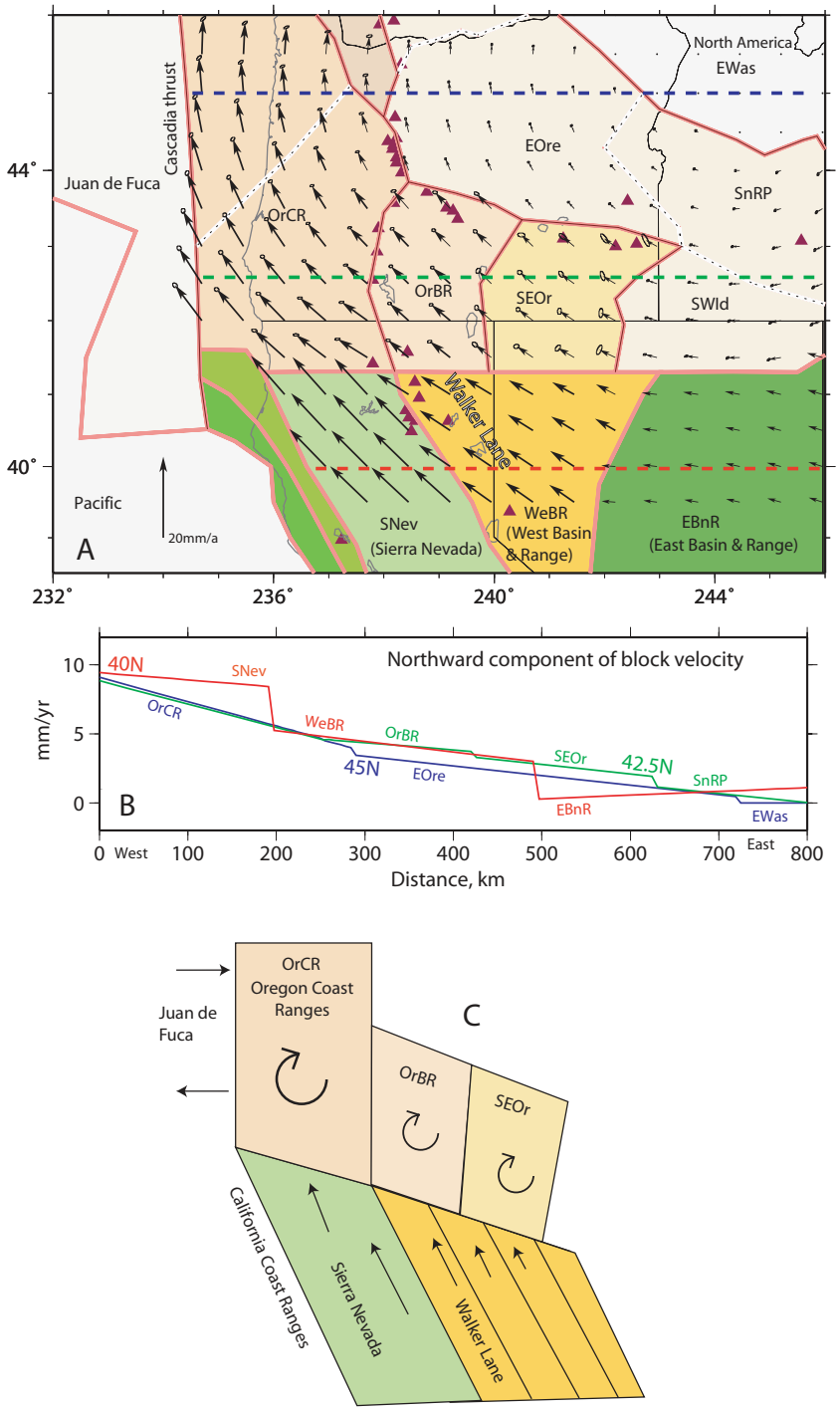

Figure 14. (a) Map of northwestern US showing rotational velocities relative to North America derived from the block model. Motions of the southern blocks (Sierra Nevada, Western Basin and Range and Eastern Basin and Range) are taken from McCaffrey (2005). The boundaries between these blocks and the Oregon blocks are uncertain. Coloured dashed lines are locations of profiles in 14b. (b) Variation of northward component of velocity across 40° N (red), 42.5° N (green) and 45° N (blue). At 40° N, the westward increase in northward velocity is largely accommodated by faulting (steps in red curve) while in Oregon the change is accommodated largely by rotations and little faulting (relatively small offsets in green and blue curves). (c) Block diagram showing how shear in the Walker Lane belt may drive rotation of the southeastern Oregon blocks (OrBR and SEOr) and how northward push of the Sierra Nevada block and clockwise torque due to subduction may rotate the Oregon Coast Ranges.

(Jones *et al*. 1996). The westward motion of southeastern Oregon is presumably driven by the opening of the northern Basin and Range. The clockwise rotation of the southern Oregon backarc (Fig. 14a; blocks OrBR and SEOr) is probably driven by the shear deformation in the Walker Lane belt. The velocity gradients across the OrBR and SEOr blocks (Fig. 14b, green line) are the same as the gradient across the WeBR block. However the gradients in the northern blocks are due to rotation and in the southern block due to shear strain. The shearing in the Walker Lane is therefore at a rate that could be driving the rotations of the rigid blocks of southeastern Oregon

(Fig. 14c). The faster rotation of the Oregon Coast ranges (OrCR) is probably due to the faster, northward push of the Sierra Nevada block to the south and the clockwise torque arising from extension in southern Cascadia and conmpression in northern Cascadia (Fig. 14c) (Humphreys & Cobblentz 2007). Though the boundary between the OrCR and Sierra Nevada blocks is uncertain (Williams *et al*. 2006), if it trends NW like most structures in the region, the sense of drag on it will be right-lateral and will add to the clockwise torque on the OrCR block.

6 CONCLUSIONS

A new GPS-derived surface velocity field for the US Pacific Northwest and southwest Canada (British Columbia) reveals broad regions of fairly rigid, block-like behaviour and other regions of distributed deformation on closely spaced faults. The GPS velocity field itself cannot resolve the slip distribution on the closely-spaced faults particularly in the Puget Lowlands region where contraction from the Cascadia thrust fault strongly overprints short wavelength strain rate variations that may arise from upper plate faulting. The use of geologic information is critical for understanding the distribution of slip on structures separated by only tens of kilometres. The motions of the Oregon and southwestern Washington blocks suggest that the total motion across the deforming zone (between Astoria OR and North America) is 7.1 ± 0.4 mm yr^{-1} and, because Vancouver Island appears to move relative to North America, the shortening rate across the Puget region of western Washington (Astoria to Bellingham WA) is 4.4 ± 0.3 mm yr^{-1}.

Most of eastern Oregon and southern Idaho rotates as a single entity in agreement with earlier geodetic studies. The transition from the Walker Lane shear zone of northern California/Nevada into southern Oregon appears to occur by block rotation rather than through-going shear strain. The velocity field of the southern Oregon backarc can be explained by a few rigid blocks separated by two or three normal faults that each slip at about 1 mm yr^{-1} or less. This level of deformation in the southern Oregon backarc is at the limit of the GPS velocity accuracies so that the GPS data can neither confirm nor rule out the presence of a more continuous deformation field. However, at the mm yr^{-1} level, most of the Pacific Northwest can be described by a few large, rotating, elastic crustal blocks.

ACKNOWLEDGMENTS

During the writing of this paper, Anthony I. (Tony) Qamar was killed doing field work. Tony pioneered GPS for scientific work in Washington state by installing the first geodetic continuous sites at Seattle (SEAT) and Neah Bay (NEAH) in 1995. Along with his students he conducted several early field surveys of geodetic monuments, obtaining the data that make possible the high level of accuracy in many of the velocities reported in this paper. Tony was an ever-cheerful and tireless colleague. Many people contributed to the field work over the past few years. Cheryl McCaffrey and Beth Walton opened their home year after year to provide a base camp for our surveyors as did Tony's wife, Kathleen Ellsbury. Many private landowners allowed access to and installation of geodetic markers. Tom Herring provided assistance with GAMIT and GLOBK. Herb Dragert and Stephane Mazzotti assisted with data from Canada. Additional survey-mode GPS data were provided by the US Geological Survey (USGS), Cascades Volcano Observatory (USGS), National Geodetic Survey, numerous county surveyors, Pacific Geoscience Centre, Base Mapping and Geomatic Services of British Columbia, Victoria Capital Regional District and Doug Hogarth. Continuous data are courtesy of operators of the Pacific Northwest Geodetic Array, Western Canada Deformation Array, Bay Area Regional Deformation Array and National Geodetic Survey Continuously Operating Reference Stations sites. Scripps Orbit and Permanent Array Center provided global RINEX files, precise orbits, and IGS solutions. Chuck DeMets provided unpublished spreading rates. Reviews by Wayne Thatcher and Mike Lisowski are appreciated. This research was supported at Rensselaer Polytechnic Institute (RPI) in part by the National Science Foundation (NSF) grant EAR-9814926 and the USGS, Department of the Interior, under USGS award number 99HQGR0014. At the University of Washington the work was supported by USGS awards 99HQRG0064, 00HQGR0063 and 01HQGR0162 and NSF awards EAR-9614600 and EAR-9616302. RWK was supported by a sub-award to Massachusetts Institute of Technology from NSF award EAR-0073769 at RPI. Figures were generated with GMT (Wessel & Smith 1998).

REFERENCES

Atwater, B.F., 1987. Evidence for great Holocene earthquakes along the outer coast of Washington state, *Science,* **236,** 942–944.

Atwater, B.F., Satoko, M.-R., Satake, K., Yoshinobu, T., Kazue, U. & Yamaguchi, D.K., 2005. The Orphan Tsunami of 1700-Japanese Clues to a Parent Earthquake in North America, U.S. Geological Survey Professional Paper 1707, 144 p.

Atwater, T., 1970. Implications of plate tectonics for the Cenozoic evolution of western North America, *Geol. Soc. Am. Bull.,* **81,** 3513–3536.

Beck, M.E., Jr., 1976. Discordant paleomagnetic pole positions as evidence for regional shear in the western Cordillera of North America, *Am. Jour. Sci.,* **276,** 694–712.

Bercovici, D. & Karato, S.-I., 2003. Theoretical Analysis of Shear Localization in the Lithosphere, in *Reviews in Mineralogy and Geochemistry: Plastic Deformation of Minerals and Rocks,* S.-I Vol. 51, chapter 13, pp. 387–420, eds Karato and H.-R. Wenk, Mineralogical Society of America, Washington DC.

Bock Y. *et al.,* 1997. Southern California Permanent GPS Geodetic Array: Continuous measurements of crustal deformation between the 1992 Landers and 1994 Northridge earthquakes, *J. Geophys. Res.,* **102,** 18 013–18 033.

Braunmiller, J. & Nabelek, J., 2002. Seismotectonics of the Explorer Region, *J. Geophys. Res.,* **107,** 2208, doi:10.1029/2001JB000220.

Bucknam, R.C., Hemphill-Haley, E. & Leopold, E.B., 1992. Abrupt uplift within the past 1700 years at southern Puget Sound, Washington, *Science,* **258,** 1611–1614.

Cassidy, J.F., Ellis, R.M., Karavas, C. & Rogers, G.C., 1998. The northern limit of the subducted Juan de Fuca plate system, *J. Geophys. Res.,* **103,** 26 949—26 961.

Conrey, R.M., Taylor, E.M., Donnelly-Nolan, J.M. & Sherrod, D.R., 2002. North-central Oregon Cascades; exploring petrologic and tectonic intimacy in a propagating intra-arc rift, in: Moore, George W., ed., Field guide to geologic processes in Cascadia; field trips to accompany the 98th annual meeting of the Cordilleran Section of the Geological Society of America, *Oregon Department of Geology and Mineral Industries Special Paper,* **36,** 47–90.

DeMets, C., Gordon, R.G., Argus, D.F., & Stein, S. 1994. Effects of recent revisions to the geomagnetic reversal time scale on estimates of current plate motions, *Geophys. Res. Lett.,* **21,** 2191–2194.

Dragert, H. & Hyndman, R.D., 1995. Continuous GPS monitoring of elastic strain in the northern Cascadia subduction zone, *Geophys. Res. Lett.,* **22,** 755–758.

Dragert, H., Hyndman, R.D., Rogers, G.C. & Wang, K., 1994. Current deformation and the width of the seismogenic zone of the northern Cascadia subducted thrust, *J. Geophys. Res.,* **99,** 635–668.

Dragert, H., Wang, K. & James, T.S., 2001. A silent slip event on the deeper Cascadia subduction interface, *Science,* **292,** 1525–1528.

England, P.C. & Wells, R.E., 1991. Neogene rotations and semi-continuous deformation of the Pacific Northwest continental margin, *Geology,* **19,** 978–981.

Fitch, T.J., 1972. Plate convergence, transcurrent faults and internal deformation adjacent to southeast Asia and the western Pacific, *J. Geophys. Res.,* **77,** 4432–4460.

Freund, R., 1974. Kinematics of transform and transcurrent faults, *Tectonophysics,* **21,** 93–134.

Freymueller, J.T., Cohen, S.C. & Fletcher, H.J., 2000. Spatial variations in present-day deformation, Kenai Peninsula, Alaska, and their implications, *J. Geophys. Res.,* **105,** 8079–8101.

Goldfinger, C., Kulm, L.D., Yeats, R.S., Appelgate, B., MacKay, M. & Moore, G.F. 1992. Transverse structural trends along the Oregon convergent margin: implications for Cascadia earthquake potential, *Geology,* **20,** 141–144.

Goldfinger, C., Kulm, L.D., Yeats, R.S., Hummon, C., Huftile, G.J., Niem, A.R. & McNeill, L.C., 1996. *Oblique Strike-slip Faulting of the Cascadia Submarine Forearc: The Daisy Bank Fault Zone off Central Oregon*, eds Bebout G. *et al.,* SUBCON AGU Geophysical Monograph, pp. 65–74.

Goldfinger, C., Nelson, C.H., & Johnson, J.E., 2003. Holocene earthquake records from the Cascadia subduction zone and northern San Andreas fault based on precise dating of offshore turbidites, *Annu. Rev. Earth Planet. Sci.,* **31,** 555–77.

Gromme, C.S., Beck, M.E. Jr., Wells, R.E. & Engebretson, D.C., 1986. Paleomagnetism of the Tertiary Clarno Formation and its significance for the tectonic history of the Pacific Northwest, *J. Geophys. Res.,* **19,** 14089–14104.

Hammond, W.C. & Thatcher, W., 2005. Northwest Basin and Range tectonic deformation observed with the Global Positioning System, 1999–2003, *J. Geophys. Res.,* **110,** B10405, doi:10.1029/2005JB003678.

Herring, T.A., 2004. *GLOBK: Global Kalman filter VLBI and GPS analysis program, Release 10.2,* Mass. Instit. of Technol, Cambridge.

Hildreth, W., Fierstein, J. & Lanphere, M., 2003. Eruptive history and geochronology of the Mount Baker Volcanic Field, Washington. *Geological Society of America Bulletin,* v.115, no. 6, 729–764.

Hill, D.P., Pollitz, F. & Newhall, C., 2002. Earthquake-volcano interactions, *Phys. Today,* 41–47.

Humphreys, E. & M.A. Hemphill-Haley, 1996. Causes and characteristics of Western U.S. deformation, *Geol. Soc. Amer.,* **28,** Program with abstracts.

Humphreys, E.D. & Coblentz, D.D., 2007. North America dynamics and western U. S. tectonics, *Rev. Geophys.,* in press.

Hyndman, R.D. & Wang, K., 1993. Thermal constraints on the zone of major thrust earthquake failure: The Cascadia subduction zone, *J. Geophys. Res.,* **98,** 2039–2060.

Hyndman, R.D. & Wang, K., 1995. The rupture zone of Cascadia great earthquakes from current deformation and the thermal regime, *J. Geophys. Res.,* **100,** 22 133–22 154.

Hyndman, R.D., Mazzotti, S., Weichert, D. & Rogers, G.C., 2003. Frequency of large crustal earthquakes in Puget Sound–Southern Georgia Strait predicted from geodetic and geological deformation rates, *J. Geophys. Res.,* **108,** 2033, doi:10.1029/2001JB001710.

Jones, C.H., Unruh, J.R. & Sonder, L.J., 1996. The role of gravitational potential energy in active deformation in the southwestern US, *Nature,* **381,** 37–41.

Khazaradze, G., 1999. Tectonic deformation in western Washington state from GPS measurements, *PhD thesis,* University of Washington.

Khazaradze, G., Qamar, A.I. & Dragert, H., 1999. Tectonic deformation in western Washington from continuous GPS measurements, *Geophys. Res. Lett.,* **26,** 3153–3158.

King, R.W. & Bock, Y., 2004. *Documentation of the MIT GPS Analysis Software: GAMIT Release 10.2,* Mass. Instit. of Technol, Cambridge.

Lay, T. & Schwartz, S., 2004. Comment on "Coupling Semantics and Science in Earthquake Research"', *Eos Trans. AGU,* **85,** 339–340.

Lewis, T.J., Lowe, C. & Hamilton, T.S., 1997. Continental signature of a ridge-trench-triple junction: Northern Vancouver Island, *J. Geophys. Res.,* **102,** 7767–7781.

Magill, J., Wells, R.E., Simpson, R.W. & Cox, A.V., 1982. Post 12 m.y. rotations of southwestern Washington, *J. Geophys. Res*., **87,** 3761–3776.

Mann, P., 1997. Model for the formation of large transtensional basins in zones of tectonic escape, *Geology,* **25,** 211–214.

Massey, N.W.D., MacIntyre, D.G., Desjardins, P.J. & Cooney, R.T., 2005, Digital Geology Map of British Columbia: Whole Province, B.C. Ministry of Energy and Mines, Geofile 2005–1, http://www.em.gov.bc.ca/Mining/Geolsurv/publications/GeoFiles/Gf2005–1/toc.htm

Mazzotti, S., Dragert, H., Henton, J., Schmidt, M., Hyndman, R., James, T., Lu, Y. & Craymer, M., 2003. Current tectonics of northern Cascadia from a decade of GPS measurements, *J. Geophys. Res.,* **108,** 2254, doi:10.1029/2003JB002653.

McCaffrey, R., 1995. DEFNODE users' guide, Rensselaer Polytechnic Institute, Troy, New York (http://www.rpi.edu/∼mccafr/defnode/).

McCaffrey, R., 1997. Influences of recurrence times and fault zone temperatures on the age-rate dependence of subduction zone seismicity, *J. Geophys. Res.,* **102,** 22839–22854.

McCaffrey, R., 2002. Crustal block rotations and plate coupling, in *Plate Boundary Zones,* Vol. 30, pp. 101–122, eds S. Stein & J. Freymueller, *AGU Geodynamics Series*.

McCaffrey, R., 2005. Block kinematics of the Pacific—North America plate boundary in the southwestern US from inversion of GPS, seismological, and geologic data, *J. Geophys. Res.,* **110,** B07401, doi:10.1029/2004JB003307.

McCaffrey, R., Long, M., Goldfinger, C., Zwick, P.C., Nabelek, J.L., Johnson, C.K. & Smith, C., 2000a. Rotation and plate locking at the southern Cascadia subduction zone, *Geophys. Res. Lett.,* **27,** 3117–3120.

McKenzie, D. & Jackson, J., 1983. The relationship between strain rates, crustal thickening, paleomagnetism, finite strain, and fault movements within a deforming zone, *Earth planet. Sci. Lett.,* **65,** 182–202.

McClusky, S. & 27 others, 2000. Global Positioning System constraints on plate kinematics and dynamics in the eastern Mediterranean and Caucasus, *J. Geophys. Res.,* **105,** 5695–5719.

McCrory, P.A., Blair, J.L., Oppenheimer, D.H. & Walter, S.R., 2003. Depth to the Juan de Fuca slab beneath the Cascadia subduction margin: A 3-D model for sorting earthquakes: *U.S. Geological Survey Digital Data Series*, 1 CD-ROM.

Miller, M.M., Johnson, D.J., Rubin, C.M., Dragert, H., Wang, K., Qamar, A.I. & Goldfinger, C., 2001. GPS-determination of along-strike variation in Cascadia margin kinematics: Implications for relative plate motion, subduction zone coupling, and permanent deformation, *Tectonics,* **20,** 161–176.

Miller, M.M., Melbourne, T., Johnson, D.J. & Sumner, W.Q., 2002. Periodic slow earthquakes from the Cascadia subduction zone, *Science,* **295,** 2423.

Mitchell, C.E., Vincent, P., Weldon, R.J. & Richards, M.A., 1994. Present day vertical deformation of the Cascadia margin, Pacific Northwest, United States, *J. Geophys. Res.,* **99,** 12 257–12 277.

Murray, M. & Lisowski, M., 2000. Strain accumulation along the Cascadia subduction zone, *Geophys. Res. Lett.,* **27,** 3631–3634.

Nabelek, J.L. & McCaffrey, R., 2001. Seismological and geodetic observations of the 28 February, 2001 Nisqually, Washington earthquake, Poster E10, *Seismol. Soc. Amer.* abstracts with Programs.

Nathan, S., 2005. *Harold Wellman: A Man Who Moved New Zealand,* pp. 272, Victoria University Press, Wellington.

Nelson, A. *et al.,* 1995. Radiocarbon evidence for extensive plate-boundary rupture about 300 years ago at the Cascadia subduction zone, *Nature,* **378,** 371–374.

Nelson, A.R., Johnson, S.Y., Kelsey, H.M., Wells, R.E., Sherrod, B.L., Pezzopane, S.K., Bradley, Lee-Ann, & Koehler, R.D., III, 2003. Late Holocene earthquakes on the Toe Jam Hill fault, Seattle fault zone, Bainbridge Island, Washington, *Geol. Soc. Amer. Bull.,* **115,** 1388–1403.

Okada, Y., 1985. Surface deformation due to shear and tensile faults in a half-space, *Bull. Seismol. Soc. Amer.,* **75,** 1135–1154.

Okada, Y., 1992. Internal deformation due to shear and tensile faults in a half-space, *Bull. Seismol. Soc. Amer.,* **82,** 1018–1040.

Pazzaglia, F.J. & Brandon, M.T., 2001. A fluvial record of long-term steady-state uplift and erosion across the Cascadia Forearc High, Western Washington State, *Am. J. Sci.,* **301,** 385–431.

Pezzopane, S.K. & Weldon, R., 1993. Tectonic role of active faulting in central Oregon, *Tectonics,* **12,** 1140–1169.

Prawirodirdjo, L. *et al.,* 1997. Geodetic observations of interseismic strain segmentation at the Sumatra subduction zone, *Geophys. Res. Lett.,* **24,** 2601–2604.

Press, W.H., Flannery, B.P., Teukolsky, S.A. & Vetterling, W.T., 1989. *Numerical Recipes,* Cambridge Univ. Press, Cambridge.

Raisz, E., 1945. The Olympic-Wallowa lineament, *Am. J. Sci.,* **243-A,** 479–485.

Reilinger, R. & Adams, J., 1982. Geodetic evidence for active landward tilting of the Oregon and Washington coastal areas, *Geophys. Res. Lett.,* **9,** 401–403.

Satake, K., Wang, K. & Atwater, B.F., 2003. Fault slip and seismic moment of the 1700 Cascadia earthquake inferred from Japanese tsunami descriptions, *J. Geophys. Res.,* **108,** 2535, doi:10.1029/2003JB002521.

Savage, J.C., 1983. A dislocation model of strain accumulation and release at a subduction zone, *J. Geophys. Res.,* **88,** 4984–4996.

Savage, J.C., Lisowski, M. & Prescott, W.H., 1991. Strain accumulation in western Washington, *J. Geophys. Res.,* **96,** 14 493–14 507.

Savage, J.C., Svarc, J.L., Prescott, W.H. & Murray, M.H., 2000. Deformation across the forearc of the Cascadia subduction zone at Cape Blanco, Oregon, *J. Geophys. Res.,* **105,** 3095–3102.

Savage, J.C., Gan, W. & Svarc, J.L., 2001. Strain accumulation and rotation in the eastern California shear zone, *J. Geophys. Res.,* **106,** 21 995–22 007.

Scholz, C., 1990. *The Mechanics of Earthquakes and Faulting,* 439 Cambridge Univ. Press, Cambridge.

Sheriff, S.D., 1984. Paleomagnetic evidence for spatially distributed post-Miocene rotation of western Washington and Oregon, *Tectonics,* **3,** 397–408.

Sherrod, D.R. & Smith, J.G., 2000. Geologic map of upper Eocene to Holocene volcanic and related rocks of the Cascade Range, Oregon: U.S. Geological Survey, Geologic Investigations Series – I-2569.

Siebert, L. & Simkin, T. (2002). Volcanoes of the World: an Illustrated Catalog of Holocene Volcanoes and their Eruptions. Smithsonian Institution, Global Volcanism Program Digital Information Series, GVP-3, (http://www.volcano.si.edu/world/).

Simpson, R.W. & Cox, A.V., 1977. Paleomagnetic evidence for tectonic rotation of the Oregon Coast Range, *Geology,* **5,** 585–598.

Steblov, G.M. *et al.,* (2003), Imprint of the North American plate in Siberia revealed by GPS, *Geophys. Res. Lett.,* **30,** doi:10.1029/2003GL017805.

Svarc, J.L., Savage, J.C., Prescott, W.H. & Murray, M.H., 2002. Strain accumulation and rotation in western Oregon, and southwestern Washington, *J. Geophys. Res.,* **107,** doi: 10.1029/2001JB000625.

Szeliga, W., Melbourne, T.I., Miller, M.M. & Santillan, V.M., 2004. Southern Cascadia episodic slow earthquakes, *Geophys. Res. Lett.,* **31,** L16602, doi:10.1029/2004GL020824.

Tabor, R.W., Haugerud, R.A., Hildreth, W. & Brown, E.H., 2003, Geologic map of the Mount Baker 30- by 60 minute quadrangle, Washington, U.S. Geological Survey, Geologic Investigation Series, I-2660, with pamphlet, 70 p., scale 1:100000, http://pubs.usgs.gov/imap/i2660/

U.S. Geological Survey, 2006. Quaternary fault and fold database for the United States, http//earthquakes.usgs.gov/regional/qfaults/.

Wallace, L.M., Beavan, J., McCaffrey, R. & Darby, D., 2004. Subduction zone coupling and tectonic block rotations in the North Island, New Zealand, *J. Geophys. Res.,* **109,** doi:10.1029/2004JB003241.

Wallace, L.M., McCaffrey, R., Beavan, J. & Ellis, S., 2005. Rapid microplate rotations and back-arc rifting at the transition between collision and subduction, *Geology,* **33,** 857–860.

Wallace, L.M., Beavan, J., McCaffrey, R. & Berryman, K., 2006. Balancing the plate motion budget in the South Island, New Zealand using GPS, geological and seismological data, *Geophys. J. Int.,* Vol. 168, no. 1, pp. 332–352. doi:10.1111/j.1365–246X.2006.03183.x.

Wang, K., 1996. Simplified analysis of horizontal stresses in a buttressed forearc sliver at an oblique subduction zone, *Geophys. Res. Lett.,* **23,** 2021–2024.

Wang, K. & Dixon, T., 2004. Coupling semantics and science in earthquake research, *Eos Trans. AGU,* **85**(18), 180.

Wang, K., Wells, R., Mazzotti, S., Hyndman, R.D. & Sagiya, T. 2003. A revised dislocation model of interseismic deformation of the Cascadia subduction zone, *J. Geophys. Res.,* **108,** 2026, doi:10.1029/2001JB001227.

Washington Division of Geology and Earth Resources staff, 2003, Digital 1:100000-scale Geology of Washington State, version 1.0, Washington Division of Geology and Earth Resources Open File Report 2005–3, http://www.dnr.wa.gov/geology/dig100k.htm

Weldon, R.J. II, Fletcher, D.K., Weldon, E.M., Scharer, K.M. & P.A. McCrory, 2003. An Update of Quaternary Faults of Central and Eastern Oregon, U.S. Geological Survey Open-File Report 02–301, Version 1.0, http://geopubs.wr.usgs.gov/open-file/of02–301/.

Wells, R.E., 1981. Geologic map of the eastern Willapa Hills, Cowlitz, Lewis, Pacific, and Wahkiakum Counties, Washington: U.S. Geological Survey Open-file Report 81–674, scale 1:62500.

Wells, R.E., 1989. Geologic map of the Cape Disappointment-Naselle River area, Pacific and Wahkiakum Counties, Washington: U.S. Geological Survey Miscellaneous Investigations Map I-1832, scale 1:62500.

Wells, R.E. & Coe, R.S., 1985. Paleomagnetism and geology of Eocene volcanic rocks of southwest Washington, implications for mechanisms of tectonic rotation, *J. Geophys. Res.,* **90,** 1925–1947.

Wells, R.E., Snavely, P.D. Jr., Macleod, N.S., Kelly, M.M., Parker, M.J., Fenton, J. & Felger, T., 1995. Geologic map of the Tillamook Highlands, northwest Oregon Coast Range-a digital database: U. S. Geological Survey Open-File Report 95–670, at: http://pubs.usgs.gov/of/1995/of95–670/.

Wells, R.E. & Heller, P.L. , 1988. The relative contribution of accretion, shear, and extension to Cenozoic tectonic rotation in the Pacific Northwest, *Geol. Soc. Amer. Bull.,* **100,** 325–389.

Wells, R.E., Weaver, C.S. & Blakely, R.J., 1998. Fore arc migration in Cascadia and its neotectonic significance, *Geology,* **26,** 759–762.

Wernicke, B.P., Friedrich, A.M., Niemi, N.A., Bennett, R.A. & Davis, J.L., 2000. Dynamics of plate boundary fault systems from Basin and Range Geodetic Network (BARGEN) and geologic data, *GSA Today,* **10,** 1–3.

Wessel, P. & Smith, W.H.F., 1998. New, improved version of the Generic Mapping Tools released, *Eos Trans. AGU,* **79,** 579.

Williams, C.A. & McCaffrey, R., 2001. Stress rates in the central Cascadia subduction zone inferred from an elastic plate model, *Geophys. Res. Lett.,* **28,** 2125–2128.

Williams, S.D.P., Bock, Y., Fang, P., Jamason, P., Nikolaidis, R.M., Prawirodirdjo, L., Miller, M. & D.J. Johnson, 2004. Error analysis of continuous GPS position time series, *J. Geophys. Res.,* **109,** B03412, doi:10.1029/2003/JB002741.

Williams, T.B., Kelsey, H.M. & Freymueller, J.T., 2006. GPS-derived strain in northwestern California: Termination of the San Andreas fault system and convergence of the Sierra Nevada—Great Valley block contribute to southern Cascadia forearc contraction, *Tectonophysics,* **413,** 171–184.

Wilson, D.S., 1993. Confidence intervals for motion and deformation of the Juan de Fuca plate, *J. Geophys. Res.,* **98,** 16 053–16 071.

SUPPLEMENTARY MATERIAL

The following supplementary material is available for this article:

Appendix S1. Supplementary appendices, tables and fault node information (PDF file).

This Material is available as part of the online article from: http://www.blackwell-synergy.com/doi/abs/10.1111/j.1365-246X.2007.03371.x (this link will take you to the article abstract).

Please note: Blackwell Publishing are not responsible for the content or functionality of any supplementary materials supplied by the authors. Any queries (other than missing material) should be directed to the corresponding author for the article.